Oliver Maier

T_1-mapping from Variable Flip Angle Data Utilizing Constrained Model-based Reconstruction

Master Thesis

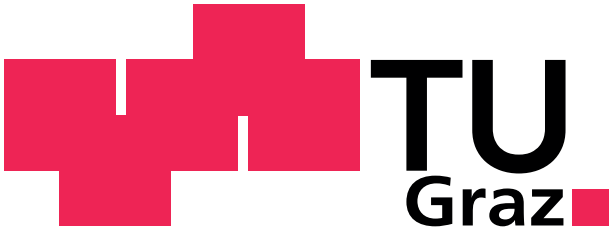

Institute for Medical Engineering
Technical University of Graz
Kronesgasse 5/II
A-8010 Graz
Head of the Institute: Univ.-Prof. Dr.techn. Dipl.-Ing. Rudolf Stollberger

Advisor:
Reviewer: Univ.-Prof. Dipl.-Ing. Dr.techn. Rudolf Stollberger

Graz, (January 20, 2016)

Acknowledgments

I owe thanks to Prof. Dr. Rudolf Stollberger for facilitating and supervising this master thesis.

A special thank goes to Matthias Schlögl for his expert guidance and support during all stages of this thesis.

Also thanks to my colleagues at the Institute of Medical Engineering at Technical University of Graz, Andreas Lesch, Andreas Petrovic, Christian Gösweiner, Christoph Aigner, Isabella Radl, Markus Bödenler, Matthias Schlögl and Stefan Span, for their support.

I would like to thank my parents, Monika and Walter, who gave me the opportunity to study and supported me all those years and my brother Manuel for his support.

Furthermore, I would like to thank my partner Karin Weninger for supporting me and providing feedback to this work.

In addition I would like to thank everyone who support me in writing this thesis.

Abstract

Quantitative imaging techniques are a main topic of ongoing research in Magnetic Resonance Imaging (MRI). Current challenges involve the speed up of acquisition as well as maintaining good accuracy. The present work describes a new accelerated T_1 mapping method on the basis of model-based reconstruction for Variable Flip Angle (VFA) data. The reconstruction problem is solved with an Iterative Regularized Gauss-Newton (IRGN)-Total-Generalized-Variation (TGV) algorithm. Reconstructed parameter maps for numerical, phantom, and in vivo knee data were in reasonable agreement with reference values up to a 12 fold acceleration. In order to minimize systematic errors it is crucial to have knowledge of the exact flip angle distribution. The blurring at sharp NMR-parameter changes provides an area for future improvements. In this context the influence of the regularization functional could be subject of further investigations.

Keywords: MRI parameter mapping, IRGN, TGV, VFA, inverse problems, primal-dual

Kurzfassung

Quantitative Bildgebungsverfahren sind ein Schwerpunktthema aktueller Forschung im Bereich MRI. Aktuelle Herausforderungen beinhalten die Beschleunigung der Aufnahme bei gleich bleibender oder besserer Genauigkeit. Die vorliegende Arbeit beschreibt ein neues, beschleunigtes Verfahren zur Bestimmung von T_1 ausgehend von einem Modell basierten Rekonstruktionsverfahren anhand von VFA Daten. Das Rekonstruktionsproblem wird dabei mittels eines IRGN-TGV Algorithmus gelöst. Die rekonstruierten Paramtermaps für numerische, Phantom und in vivo Daten waren bis zu einem Beschleunigungsfaktor von 12 in guter Übereinstimmung mit den Referenzwerten. Um möglichst kleine systematische Fehler zu erhalten ist die genaue Kenntnis der aktuellen Kippwinkel notwendig. Die Unschärfen bei starken NMR-Parameteränderungen stellen einen Bereich für zukünftige Verbesserungen dar. In diesem Zusammenhang könnten die Einflüsse durch das Regularisierungsfunktional noch weiter untersucht werden.

Schlüsselwörter: MRI parameter mapping, IRGN, TGV, VFA, Inverse Probleme, primal-dual

Contents

Statutory Declaration

I declare that I have authored this thesis independently, that I have not used other than the declared sources / resources, and that I have explicitly marked all material which has been quoted either literally or by content from the used sources.

Eidesstattliche Erklärung

Ich erkläre an Eides statt, dass ich die vorliegende Arbeit selbstständig verfasst, andere als die angegebenen Quellen/Hilfsmittel nicht benutzt und die den benutzten Quellen wörtlich und inhaltlich entnommene Stellen als solche kenntlich gemacht habe.

Ort	Datum	Unterschrift

Abbreviations

T_E Echo Time.

T_I Inversion time.

T_R Repetition Time.

BFGS Broyden-Fletcher-Goldfarb-Shanno.

bSSFP balanced Steady-State Free Precession.

CG Conjugate Gradient.

CG-descent Non-Linear Conjungate Gradient.

CPMG Carr Purcell Meiboom Gill Sequence.

CT Computer Tomography.

DESPOT Driven Equilibrium Single Pulse Observation of T_1,T_2.

FID Free Induction Decay.

FLAIR Fluid-Attenuated Inversion Recovery.

FLASH Fast Low Angle Shot.

IR Inversion Recovery.

IRGN Iterative Regularized Gauss-Newton.

LBFGS Limited-Memory Broyden-Fletcher-Goldfarb-Shanno.

LL Look-Locker.

MOLLI Modified Look-Locker Inversion Recovery.

MRF Magnetic Resonance Fingerprinting.

MRI Magnetic Resonance Imaging.

NMRS Nuclear Magnetic Resonance Spectroscopy.

PD Proton Density.

RF Radio Frequency.

SAR Specific Absorption Rate.

SENSE Sensitivity Encoding.

SNR Signal-To-Noise Ratio.

STIR Short-Tau Inversion Recovery.

TGV Total-Generalized-Variation.

TrueFISP True Fast Imaging With Steady State Precession.

TV Total-Variation.

VFA Variable Flip Angle.

1 Introduction

MRI is widely used in clinical routine diagnostics due to its excellent soft-tissue contrast providing a vital diacritic tool for physicians. Compared to Computer Tomography (CT) diagnostics, MRI offers better soft-tissue contrast without any radiation exposure for the patients. On the other hand CT has the advantage of image contrast based upon a physical quantity, the Hounsfield unit, enabling the computation of appropriate transfer functions (e.g. for volume rendering) because the specific value of the tissue is known in advance. CT is also a faster scanning technique. In contrast to CT, MRI offers only relative tissue contrast because the contrast is based upon multiple factors such as MRI sequence type, repetition time, and flip angle.

Commonly used imaging techniques in MRI try to generate image contrasts like the so called T_1-weighted, T_2-weighted, or Proton Density (PD)-weighted images. However, these images are usually a combination of all three weightings. An image is called T_1-, respectively T_2- or PD-weighted if the difference or change in T_1,(T_2, PD) contributes the most to changes in image contrast. In-vivo, the intensity values of pixels containing the same tissue can be diverse depending on the used imaging sequence and imaging parameters such as Fluid-Attenuated Inversion Recovery (FLAIR)(suppressing the water signal) and Short-Tau Inversion Recovery (STIR)(suppressing the fat signal), coil sensitivity, the used imaging hardware, B_1-inhomogeneities, B_0-inhomogeneities, rapid susceptibility changes, and partial volume effects yielding only relative contrast. To overcome this drawback researchers are developing methods to quantify physical parameters in MRI as a post

processing step. These quantitative MRI techniques became more and more important in recent years due to the increasing computing capability of computers and increased precision and speed of the MRI hardware.

Quantitative MRI offers the possibility of measuring physical quantities rather than relative contrast depending on the used sequence. Possible quantities for an MRI parameter map are for example the longitudinal relaxation time constant T_1, the transversal relaxation time constant T_2 and the proton density PD. Absolute PD is difficult to measure and is commonly replaced by a relative measurement named M_0. These quantities are characteristic for a specific type of tissue but also depend on environment variables such as temperature, static field strength B_0, and other. Different techniques exist to identify these parameters which will be presented in the following chapters. A possible application for quantitative MRI are quantitative tracer kinetic studies. These are techniques to measure vascular parameters such as blood volume and capillary permeability using dynamic contrast-enhanced MR data. In order to obtain accurate results it is crucial to obtain accurate T_1-maps of the tissue in advance. A major part of such studies is the calibration of the tracer kinetic model which depends strongly on the pre-contrast tissue T_1 [5, 4, 3, 2, 1]. In order to characterize a lesion precisely, locate small lesions or investigate multiple lesions, a 3D tracer kinetic study is necessary which presupposes a 3D T_1 map. Acquiring 3D T_1-maps with sub-millimeter resolution is very time consuming, therefore fast imagine techniques are needed.

T_1-mapping in combination with a radiation sensitive gel can be used as radiation dosimetry because the T_1 of the gel is inversely proportional to the dose of ionizing radiation[6] enabling high resolution 3D radiation dosimetry. These measurements can be used as a quality control tool in cancer radiation therapy. Parameter mapping offers huge possibilities for characterization of tissue and classification and quantification of diseases. The reason why it is not used in every day routine diagnostics is the relatively long scan time. Since faster imaging strategies are already limited by hardware constraints, Specific Absorption Rate (SAR) safety limits, and nerve stimulation limits, further scan time re-

duction is only achieved with undersampling strategies. In order to remove the artifacts induced with the incomplete data problem, more sophisticated reconstruction methods are necessary and are the focus of this work in the context of gaining quantitative information.

The two main research fields are the so called the fingerprinting and the model-based reconstruction. The former uses a huge database including all possible combination regarding the parameters of interest and a search for the combination of those which match the measured signal best, see section 1.1.6 for details. The model-based reconstruction makes use of the signal equation corresponding to the used imaging sequence and an optimization algorithm which minimizes the difference between measured signal and model generated data. Once the difference is minimized the identified model parameters represent a good approximation of the underlying physical parameters of the tissue. In order to provide the reader a quick overview of the huge field of parameter mapping a selection of existing methods is given in the following chapter.

1.1 Background

1.1.1 Relaxation, T_1, T_2 and ρ

In MRI the term longitudinal relaxation is used to describe the return of the magnetization to the thermodynamical equilibrium which is aligned with the static magnetic field B_0. This direction is arbitrary chosen to be the z-axis. Transverse relaxation on the other hand describes the loss of coherence of the spins by dephasing. Assuming a 90° excitation the magnetization is tilted 90° and the net magnetization lies in the x-y-plane. After such an excitation pulse all spins in a sample are aligned in a specific direction and in phase and a net magnetization can be measured. This net magnetization rotates in the x-y-plane with a nuclei specific frequency named Lamor-frequency (ω_L). It is dependent on the static magnetic field B_0 and the gyromagnetic constant $\gamma_{H^+} = 42.5781\,MHz/T$ of

the material and can be calculated by Equation 1.1.

$$\omega_L = \gamma B_0 \tag{1.1}$$

This transversal magnetization decays very fast because of spin-spin interactions leading to slightly different rotation frequencies. These differences lead to a dephasing of the spins ultimately canceling out each other. This effect is described by a mono-exponential function 1.5 with a time constant T_2 therefore the name T_2 decay, see Figure 1.2(a) and 1.1. Due to technical reasons like field inhomogeneities this effect is even more pronounced which results in a faster decay with a time constant T_2^*, see Equation 1.2.

$$\frac{1}{T_2^*} = \frac{1}{T_2} + \frac{1}{T_{2'}} \tag{1.2}$$

The measured signal is called Free Induction Decay (FID). Assuming no energy is lost during this process (very long T_1 compared to T_2) the majority of spins is still in an upper energy state. In order to return to the thermodynamical equilibrium they have to dissipate energy to the lattice which converts the energy to thermal energy and dissipates it via heat. This process is called spin-lattice relaxation or longitudinal relaxation and can also be described by a mono-exponential function 1.3 with a time constant T_1, therefore it is known as T_1 relaxation, see Figure 1.2(b). These two effects are specific for a given substance and can be used to generate quantitative images (parameter map). Another important factor is the proton density PD, usually denoted as ρ, which describes the number of spins per pixel/voxel. The more proton spins within the sample volume the higher the signal and the better the Signal-To-Noise Ratio (SNR).

$$S = k\rho(1 - e^{-\frac{T_R}{T_1}}) \tag{1.3}$$

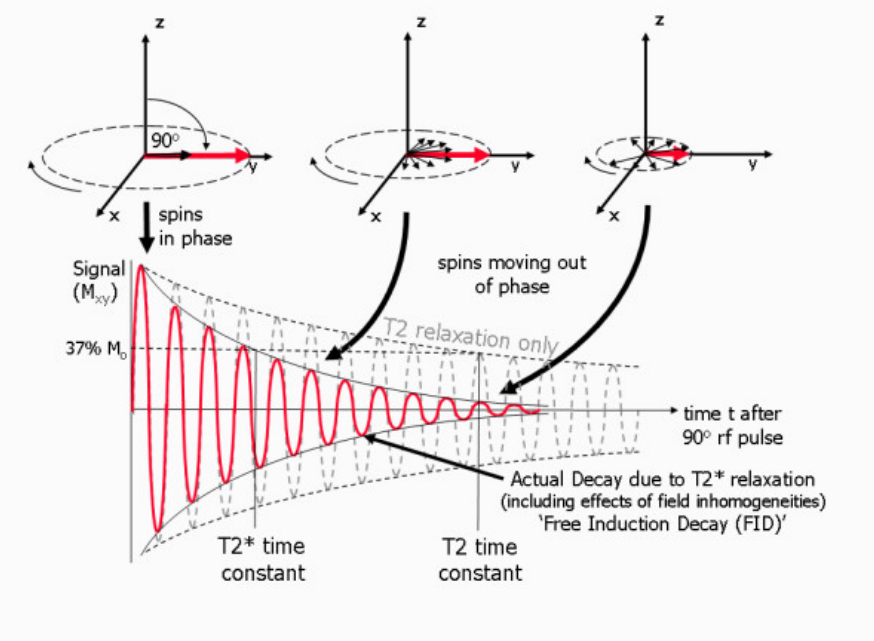

Figure 1.1: Signal decay T_2 and T_2^* for a 90° excitation pulse without T_1 decay. Figure taken from http://www.jcmr-online.com/content/12/1/71/figure/F4.

1.1.2 Classic T_2 and T_1 mapping techniques

The described techniques in this section are conventionally applied but typically suffer from very long acquisition times due to the need of long Repetition Time (T_R). The oldest uses the basic spin echo signal equation 1.4

$$S = k\rho(1 - e^{-\frac{T_R}{T_1}})e^{-\frac{T_E}{T_2}} \tag{1.4}$$

where k is a scaling factor. Acquiring T_2 weighted images($T_R \gg T_1$,T_R T_2) the signal equation 1.4 becomes 1.5 and the signal at different Echo Time (T_E)s follows a mono-exponential decay with increasing T_E, see Figure 1.2(a).

$$S = k\rho e^{-\frac{T_E}{T_2}} \tag{1.5}$$

The usage of a multi spin echo sequence (e.g. Carr Purcell Meiboom Gill Sequence (CPMG)) with different T_E or a single spin echo experiment with different echo spacing

τ and a fitting technique, for example minimum-least-squares, results in a T_2 parameter map.

A commonly used T_1 mapping technique is the Inversion Recovery (IR) spin echo sequence, where T_1 relaxation takes place between an inversion pulse and the following excitation. The condition $T_R \gg T_1$ has to be fulfilled in order to make sure all spins are in equilibrium before the next excitation. In this special case the signal after the inversion pulse can be described by 1.6 depending on the Inversion time (T_I) and follows a mono-exponential curve shown in Figure 1.2(b). This sequence yields a very good T_1 contrast.

$$S = k\rho(1 - 2e^{-\frac{T_I}{T_1}}) \tag{1.6}$$

Acquiring images at different T_I's and using a fitting routine as mentioned before yields a T_1 parameter map.

These fitting techniques are simple to compute but are time consuming if a 3D-volume with high spatial resolution should be examined due to the lengthy imaging sequences used (e.g. IR-SE sequence with 256x256 matrix and $T_R = 3s$ leads to a scan time of approximately 12 min per slice and T_I). In order to achieve an accurate fit, data from at least six points should be available. Before each excitation, the magnetization has to be in equilibrium which is generally achieved after waiting approximately five times T_1, which lies in the range of 10s. This demand for equilibrium is the reason for the long acquisition time. Multi spin echo sequences for T_2 mapping offer shorter scan time compared to single spin echo sequences but suffer from stimulated echos, imperfect slice profile, and B_1 inhomogeneities leading to errors in the estimated parameters. This is the reason why single spin echo sequences still represent the current gold standard. Lengthy imaging sequences are a major drawback in clinical routine diagnostic where scan time per patient is a crucial factor. The majority of people who need to be examined by MRI are elderly and sick people who can not stay in the scanner over a longer period. Clinical usable examination protocols should not exceed the 30 minute mark which is considered

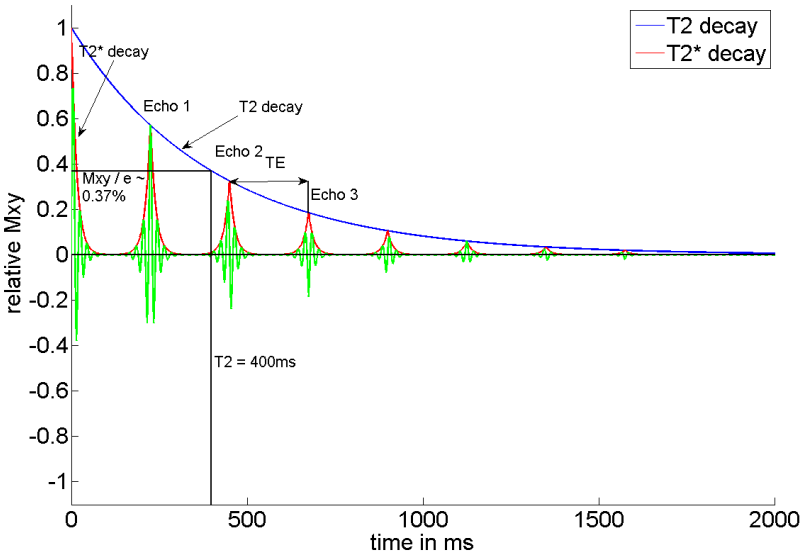

(a) T2 decay

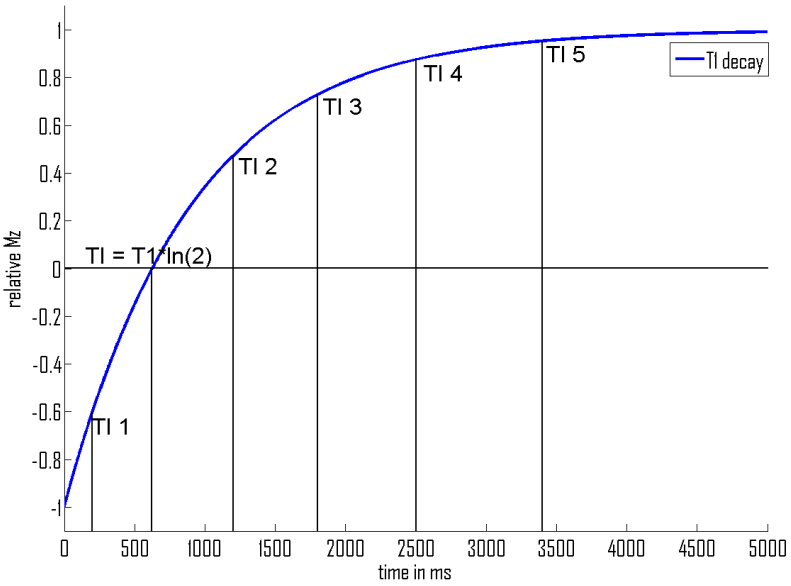

(b) T1 decay

Figure 1.2: Signal decay of T_2 for multi spin echo 1.2(a) and T_1 for Inversion Recovery 1.2(b) sequence. Multiple Echos and Inversion times are shown as an example for properly chosen time points to fit the mono-exponential curve.

a reasonable time most patients can tolerate [7]. In order to meet this time limitation

combined with a fit as accurate as possible, imaging sequence utilizing high acceleration and complex reconstruction algorithms are being developed.

1.1.3 Look-Locker methods

These methods are based on the fact that it is not necessary to wait for equilibrium magnetization before starting the next image acquisition train. Look and Locker derived an explicit formulation for calculating the magnetization after an arbitrary number of excitations in Nuclear Magnetic Resonance Spectroscopy (NMRS) [8] which was later introduced to the MRI. After the 180°-pulse multiple echos are generated using a Fast Low Angle Shot (FLASH) sequence. This further decreases scan time but makes the method sensitive to static field inhomogeneities. In contrast to recovery methods, one shot methods use a series of small flip angle pulses to measure all points along the T_1 relaxation curve in one recovery. Using small flip angles in combination with a FLASH sequence takes away some magnetization after each excitation resulting in a modified relaxation time T_1^*, which is described by the formula of Look and Locker. Acquiring all necessary points in a single shot results in a drastic time decrease for the whole examination. Due to the limited flip angles this method yields an inferior SNR relative to the recovery method. However, the reduced scan time can be used to increase the SNR through averaging [9]. The fitting of T_1 is carried out through a three parameter fit of a mono-exponential decay 1.8 and solving for T_1 1.9. The decay is based upon a modified time constant T_1^* which depends on T_1, the time between pulses τ and α, see Equation 1.7. Using three parameters enables the correction of imperfect flip angles, leading to more accurate results. However this method is still time consuming compared to modern FLASH and balanced Steady-State Free Precession (bSSFP)-based methods.

$$T_1^* = \frac{T_1}{1 - \frac{T_1}{\tau} \ln(\cos\alpha)} \tag{1.7}$$

$$S = A - B \exp\left(\frac{-t}{T_1^*}\right) \tag{1.8}$$

$$T_1 = T_1^* \left(\frac{B}{A} - 1\right) \tag{1.9}$$

The 2D-Look-Locker method was adapted for 3D-measurements by Henderson et al. in 1999 [10]. They showed good agreement with the inversion-recovery spin echo measurements and a fast image acquisition time of approximately 8 minutes for a 256x128x32 image matrix, 5/8 partial Fourier, $\tau = 5.5ms$, and $T_R = 2000ms$. The encoding scheme for the 3D-Look-Locker is illustrated in Figure 1.1.3. However, no B_{1+}-correction was performed which would further increase the accuracy of the proposed method because of the flip angle dependence of T_1^* like in all other Look-Locker methods. Furthermore acquiring isometric resolution brain images requires an even higher matrix size which would result in scan times longer than 20 minutes, which is not feasible in clinical routine diagnostics [11].

A fast Look-Locker method that allows T_1 quantification at the heart is known as Modified Look-Locker Inversion Recovery (MOLLI) first published by Messroghli et al. [12]. This method modifies the standard Look-Locker (LL)-method by a selective data acquisition triggered by the ECG at the end of the diastole and merging of three images acquired at different T_I into one data set. A bSSFP read-out sequence is used because of its high SNR combined with a Sensitivity Encoding (SENSE) factor of two to further decrease the scan time, decreasing motion artefacts due to short acquisition compared to the heart beat rate. A disadvantage of this method is the dependency of T_1 upon the heart rate and its rather larger estimation error for very short (<180ms) and long (>1200ms) T_1, limiting the application of the method.

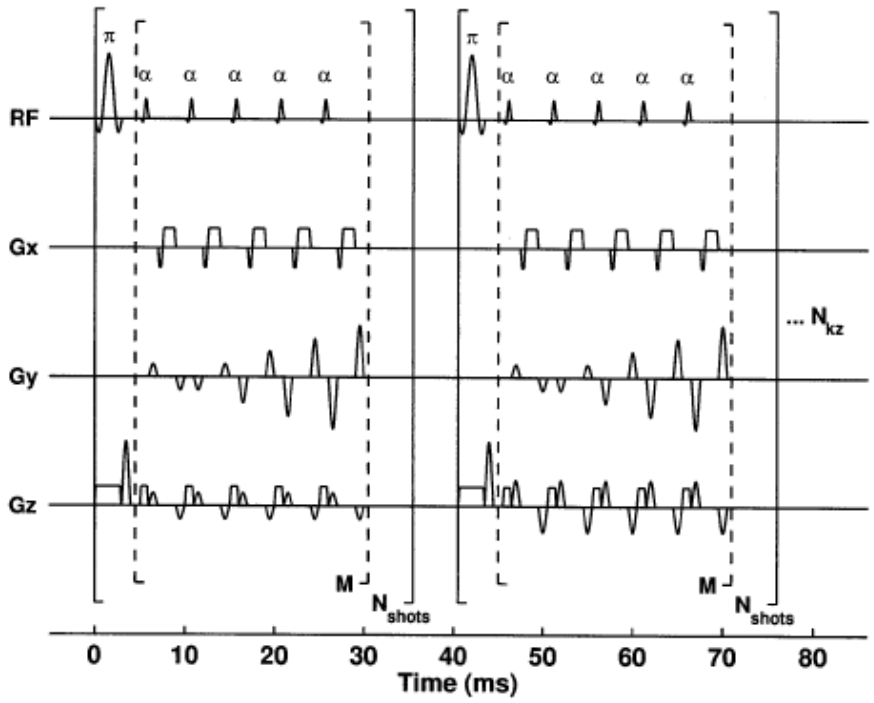

Figure 1.3: Acquisition scheme for 3D-Look-Locker sequence proposed by Henderson et al. After an inversion pulse a number k_y of phase encoding steps is performed in the inner loop. This is repeated M times until the necessary number of k_y is acquired. The outer loop N_{kz} defines the measurement volume. The flip angle α should be small, e.g. $\alpha < 15°$, in order to not drive the magnetization to equilibrium too fast. Figure taken from [10]

1.1.4 Inversion Recovery balanced Steady-State Free Precession

The IR-bSSFP, also know as IR-True Fast Imaging With Steady State Precession (True-FISP), technique was first introduced by Schmitt et al.[13] in 2004. It utilizes a inversion pulse followed by a bSSFP read out with an initial $\frac{\alpha}{2}$ preparation pulse. The transient signal for an $\frac{\alpha}{2}$ prepared bSSFP sequence can be described by a three parameter mono-exponential function 1.10, see Scheffler et al. [14].

$$S(nTR) = S_{stst}(1 - INVe^{-nTR/T_1^*}) \tag{1.10}$$

Where:

S_{stst} : The steady-state signal
T_1^* : Apparent relaxation time $\leq T_1$
INV : Inversion factor indicating the ratio between S_0 and S_{stst}
nTR : n times TR of the current read-out sequence

Schmitt et al.[13] showed that accurate values for T_1, T_2 and M_0 can be acquired with a three parameter fit of the transient signal and the use of the following equations:

$$T_1 = T_1^* \left[\cos^2 \frac{\alpha}{2} + (A \times INV + B) \sin^2 \frac{\alpha}{2}\right] \tag{1.11}$$

$$T_2 = T_1^* \left[\sin^2 \frac{\alpha}{2} + (A \times INV + B)^{-1} \cos^2 \frac{\alpha}{2}\right] \tag{1.12}$$

$$M_0 = \frac{S_{stst}\,(INV - 1)}{\sin \frac{\alpha}{2}} \tag{1.13}$$

Where:

$$A = 2\,(1 - \cos\alpha)^{-1} \cos \frac{\alpha}{2} \tag{1.14}$$

and

$$B = \left(1 + 2\cos \frac{\alpha}{2} + \cos\alpha\right) (\cos\alpha - 1)^{-1} \tag{1.15}$$

The equation for M_0 only holds if T_2 relaxation between the $\frac{\alpha}{2}$-preparation pulse and the first α-pulse can be neglected. Furthermore, it is assumed that the off-resonance frequency is zero and the magnetization evolves along the $\frac{\alpha}{2}$ cone [14].

Advantages of this method are the relative fast acquisition time, the ability to fit all three parameters using only one sequence and the good agreement with reported values in the literature. Drawbacks include its dependency upon off-resonance effects e.g. banding, rather long scan duration for tissues with high T_1 values because of the need of a steady-

state signal, the sensitivity to imperfect slice profiles, and the influence of magnetization transfer effects [15].

1.1.5 The Variable Flip Angle approach

The VFA approach is a fast and relatively accurate method utilizing variation in signal intensities based upon a variation of the flip angle to infer the unknown parameters. A well established method is the Driven Equilibrium Single Pulse Observation of T_1,T_2 (DESPOT)-approach published by Deoni et al. in 2003 [16]. This method enables the computation of T_1,T_2, and M_0 using fully sampled 3D-FLASH and bSSFP sequences in less than 20 minutes. The method, called DESPOT1, can be used to either fit T_1 and M_0, which uses the FLASH sequence to extract T_1 and M_0. DESPOT2, utilizing the bSSFP sequence is used to calculate T_2 and M_0 assuming T_1 is known. The steady-state signal for the FLASH sequence can be described by 1.16, the one of the bSSFP sequence by 1.17, where $E_1 = e^{-\frac{T_R}{T_1}}$, $E_2 = e^{-\frac{T_R}{T_2}}$ and α is the excitation flip angle. The dependency of the signal on T_1, T_2, and flip angle α for the FLASH and bSSFP sequence is shown in figures 1.4(a)- 1.4(c).

$$S_{FLASH} = \frac{M_0(1 - E_1)\sin\alpha}{1 - E_1\cos\alpha} \tag{1.16}$$

$$S_{bSSFP} = \frac{M_0(1 - E_1)\sin\alpha}{1 - E_1E_2 - (E_1 - E_2)\cos\alpha} \tag{1.17}$$

$$\frac{S_{FLASH}}{\sin\alpha} = E1\frac{S_{FLASH}}{\tan\alpha} + M_0(1 - E1) \tag{1.18}$$

$$\frac{S_{bSSFP}}{\sin\alpha} = \frac{E_1 - E_2}{1 - E_1E_2} \times \frac{S_{bSSFP}}{\tan\alpha} + \frac{M_0\,(1 - E_1)}{1 - E_1E_2} \tag{1.19}$$

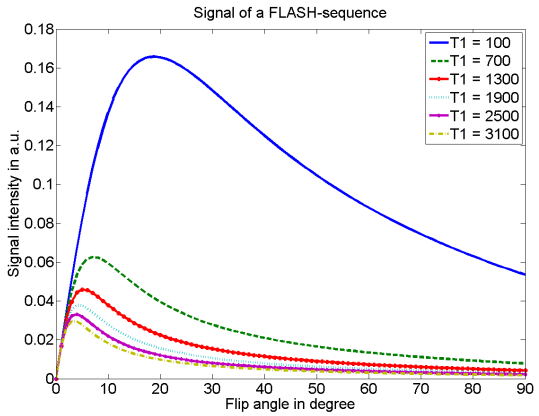

(a) Signal intensity of a FLASH sequence with varying α and T_1

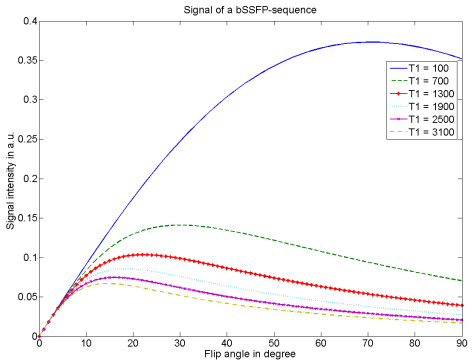

(b) Signal intensity of a bSSFP sequence with varying α and T_1

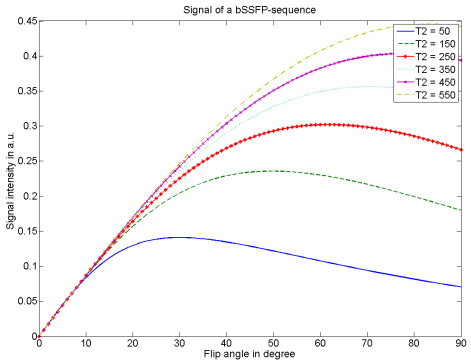

(c) Signal intensity of a bSSFP sequence with varying α and T_2

Figure 1.4: This figure shows the signal dependency of the FLASH and bSSFP sequence upon the flip angle α for different values of T_1 and T_2. For the FLASH sequence exists an specific flip angle α which maximizes the signal for a given combination of T_1 and T_R.

If T_R is kept constant and α is varied one generates images characterized by T_1 respectively T_1 and T_2, depending on the used sequence. Through rearranging the signal equations into a linear form(1.18, 1.19) and performing linear regression to calculate the slope m and intercept b it is possible to calculate T_1, T_2, and M_0:

DESPOT1:

$$T_1 = \frac{-T_R}{\ln(m)} \tag{1.20}$$

$$M_0 = \frac{b}{1-m} \tag{1.21}$$

DESPOT2, assuming T_1 is known:

$$T_2 = \frac{-T_R}{\ln\left(\frac{m-E_1}{mE_1-1}\right)} \tag{1.22}$$

$$M_0 = \frac{b\,(E_1E_2-1)}{1-E_1} \tag{1.23}$$

Deoni et al. [16] showed that it is possible to achieve an accurate fit by using two ideal flip angles. Furthermore, he derived an analytical equation to calculate those angles for the FLASH sequence:

$$\alpha = \cos^{-1}\left(\frac{f^2E_1 \pm (1-E_1^2)\sqrt{1-f^2}}{1-E_1^2(1-f^2)}\right) \tag{1.24}$$

where:

$$f = 0.71$$

For calculating the ideal flip angles for the bSSFP sequence, the interested reader is referred to [16].

The ideal number and value for the flip angles depends on the expected T_1 values. Cheng et al. [7] showed that a set of three flip angles provided the best results and thus it is best to use scan time to increase the SNR of those three scans through averaging rather than performing more scans with different flip angles. They also proposed a method to choose the flip angles based upon the maximum and minimum expected T_1 value. Furthermore,

they showed that a minimum SNR of 350 is needed to achieve accurate T_1 measurements.

The DESPOT approach is suitable to achieve high resolution parameter maps of a large volume (e.g.: 25x25x10 cm with $<1mm^3$ Voxel-size) in less than 20 minutes with precision comparable to recovery methods, see section 1.1.2. The major drawback of this method is its limited acceleration potential due to the fact, that it operates directly on the images rather than the k-space itself, limiting the acceleration factor to moderate values up to 4 combined with parallel imaging techniques. Furthermore the expected range of T_1 respectively T_2 values has to be known in advance to properly choose the ideal flip angles. The set of ideal flip angles can interfere with the proposed SNR-threshold because very small flip angles of $3°$ are needed, which in return yields images with rather poor SNR. Another drawback is the sensitivity of the method with respect to flip angle uncertainties due to imperfect slice profiles and an inhomogeneous B_{1+}-profile, leading to errors in the estimated parameters. This limitation gives rise to more sophisticated reconstruction and fitting methods.

1.1.6 Fingerprinting

Magnetic Resonance Fingerprinting (MRF) is a relatively young technique first published by Dan Ma et al. [17] in 2013. The basic assumption is that every tissue has its unique set of parameters and thus unique signal evolution, called fingerprint. MRF uses a dedicated imaging sequence to increase the distinct information in the signal evolution during the acquisition and a pattern recognition algorithm to match the fingerprint to a predefined set of predicted signal evolutions called dictionary. If the signal can be matched to a dictionary entry, it is possible to generate quantitative maps of all parameters associated with that particular entry. In order to generate an unique fingerprint it is necessary to vary imaging parameters, such as the flip angle and phase of radio frequency pulses, the repetition time, echo time and sampling pattern, in a pseudorandom manner. A possible acquisition scheme for a bSSFP sequence is shown in Figure 1.5. Advantages of MRF include its

high acceleration potential due to the fact that undersampling artefacts are suppressed by the pattern recognition algorithm. This can be achieved if the undersampling artefacts of the used pattern are mostly uncorrelated to each other. Figure 1.6 shows an example of reconstructed parameter maps using fingerprinting. In order to increase the acquired information in a given time frame the parameters are varied in such a way that no stead-state is reached. It is also more sensitive with respect to imaging and tissue parameters. In summary, this enables an acquisition speed-up of more than 30 with still excellent image quality concerning artefacts. Possible drawbacks of MRF include the lack of a proof that only one fingerprint yields the best match, and its rather high storage requirements if more parameters should be fitted, because signal behavior for all possible, allowed parameter combinations have to be precomputed and stored in a database yielding billions of entries. Another problem that comes side by side with huge databases is the need for reliant and fast matching algorithms which have to be developed.

1.1.7 Model-based Reconstruction

Model-based reconstruction makes use of the signal equation corresponding to the used sequence, in order to incorporate additional information to the minimization problem of finding the parameters of interest. The problem of finding the ideal set of parameters is solved iteratively. The data generated by the forward model is compared to the acquired data and by varying the model parameters the residual error is minimized in a least-square sense 1.25. The minimization problem at hand may be non-linear or even non-convex. Therefore, advanced algorithms are needed to find a solution. Model-based reconstruction can be used for sequences where an analytical expression for the signal exists, but could also be used with the Bloch equations.

$$\min_x \frac{1}{2}\|G(x) - d\|_2^2 \tag{1.25}$$

Where:

x : Vector of unknown parameters $\in \mathbb{R}_+^{q \times n \times m}$

q : Number of unknown parameters

d : Measured data $\in \mathbb{C}^{n \times m \times i \times k}$

i : Number of coils

k : Number of varied parameters (e.g. flip angle)

G : Function mapping the parameters $X \to Y$ which lies in data space, comprising a model of the MRI signal

Advantages of model-based reconstruction are the well known behavior of various minimization algorithms which exist to solve the problem at hand and its high acceleration potential, if these algorithms are combined with proper regularization methods. Possible drawbacks are rather long reconstruction time, depending on the used solver, and limitation of the regularization depending on the optimization algorithm. Because in this work the model-based reconstruction approach is used, a more detailed explanation of this method is given in chapter 2.

Because of the numerous advantages of model-based reconstruction it is used in a huge variety of applications. Some examples include a model-based acceleration of LL T_1 mapping proposed by Tran-Gia et al. [18] which uses model-based fitting of an exponential relaxation process to reconstruct parameter maps of highly undersampled and radially acquired IR-LL data. Another example is a model-based T_2 mapping technique proposed by Sumpf et al. [19] which utilizes a train of spin echo sequences at different T_E's to generate T_2 and spin density maps. Furthermore, model-based reconstruction is not limited to simple signal models but can also be used with the generating function formalism, see

for example [20], or even the Bloch equations, allowing very fast acquisition, e.g. by using the transient signals as the base for the parameter mapping.

1.2 Definition of task

The aim of this work is to develop and compare different algorithms in order to reconstruct parameter maps regarding T_1 using by highly undersampled FLASH data. Utilizing an existing Matlab script (Mathworks Inc., Natick, USA) as starting point and adapting it for the FLASH sequence the performance of Non-Linear Conjungate Gradient (CG-descent), Limited-Memory Broyden-Fletcher-Goldfarb-Shanno (LBFGS), and IRGN-TGV by means of computation time, correctness of fit, SNR, and memory usage should be compared. In addition to these different undersampling patterns, cartesian interleaved, radial and pseudorandom, are used and compared in terms of maximum possible image acceleration and resulting quality of fit. This comparison is carried out in three different stages. First, using numerical simulated data to proof the correctness of the implemented algorithm, secondly using MRI-phantom data, and lastly in vivo data of human knees.

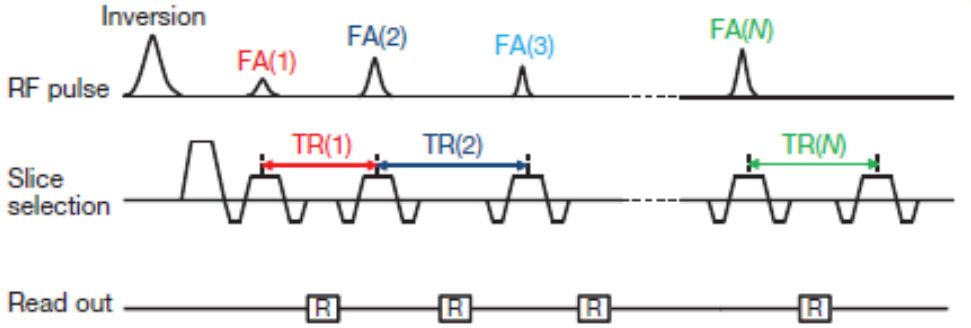

(a) sequence diagram

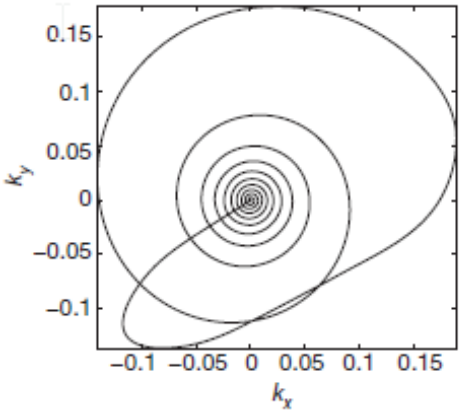

(b) sampling pattern

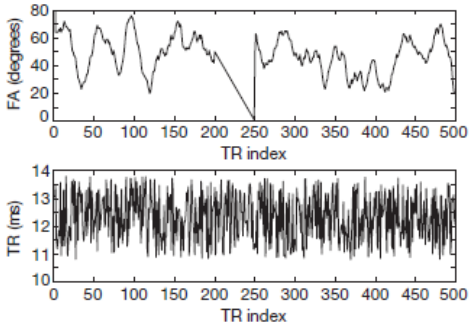

(c) varying parameters

Figure 1.5: 1.5(a) shows a bSSFP sequence diagram with varied acquisition parameters during every readout. The parameters are varied in a pseudorandom pattern. A possible pattern for the varied parameters is shown in 1.5(c). In order to maximize the k-space information and minimize undersampling artefact coherence a variable density spiral readout is used 1.5(b). Figure adopted from [17].

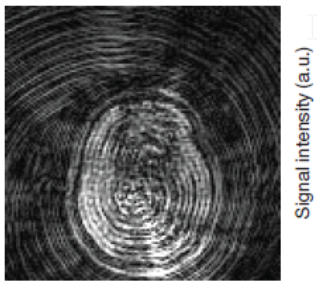

(a) reconstructed image from one acquisition

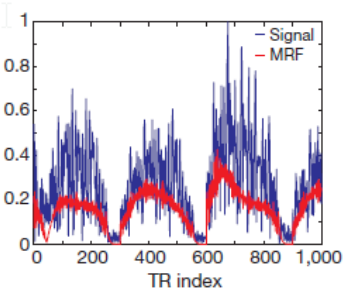

(b) matched signal of one pixel

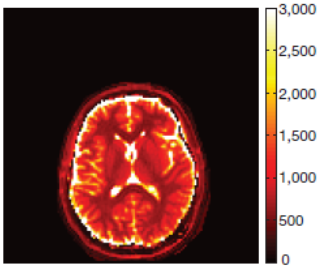

(c) T_1 map

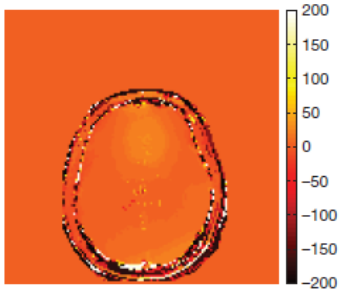

(d) off-resonance frequency

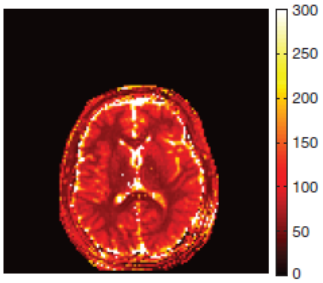

(e) T_2 map

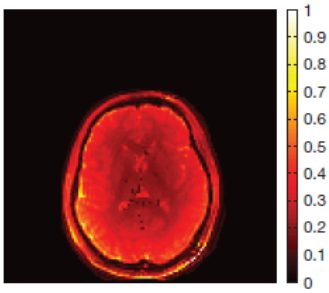

(f) M_0 map

Figure 1.6: Example of the high acceleration potential of MRF. Conventional reconstruction yields significant undersampling errors 1.6(a). Signal evolution in one Pixel 1.6(b). Reconstructed parameter maps 1.6(c)-1.6(f). Figure adopted from [17].

2 Methods

2.1 Generation of undersampled data

In order to achieve high acceleration it is necessary to reduce the scan time. This is usually done by reducing the number of phase encoding steps, effectively reducing the acquired data. Because of the nature of MRI data acquisition and the well known properties of the Fourier transform, reducing the acquired data inevitable leads to aliasing artifacts in the reconstructed image. Depending on the used undersampling pattern the artifacts are differently pronounced. One of the first undersampling strategies used is the skipping of a predefined number of lines which reduces the effective scan time by the amount of lines skipped, e.g. skipping every second line yields a effective acceleration of 2. However, this technique yields pronounced undersampling artefacts because the Nyquist criterion is violated, leading to backfolding in phase encoding direction. Another method known from CT reconstruction is radial sampling which offers the benefit of nearly uncorrelated undersampling artefacts leading to rather high quality images even at high acceleration factors. A new sampling approach is know as pseudo-random sampling which determines the sampling position by means of drawing from a 2D Poisson disc random distribution with variable density. Specifying the sampling points in a pseudo-random fashion yields highly uncorrelated artefacts which manifest as additive noise in the image, see Figure 2.1(e). The k-space is fully sampled in a 32x32 neighborhood around the center. All three methods were implemented as a preprocessing step in order to produce artificially

undersampled data from fully sampled reference scans and numerical phantoms.

(a) Reference Image

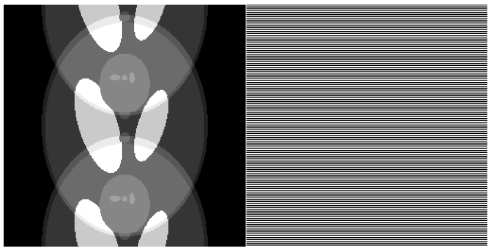

(b) interleaved AF2

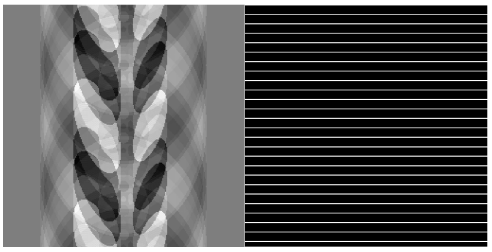

(c) interleaved AF10

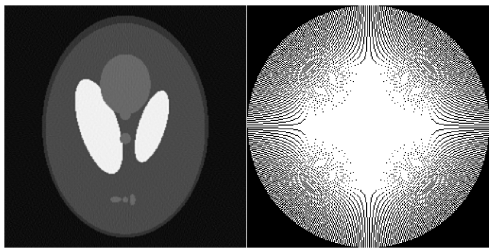

(d) radial AF2

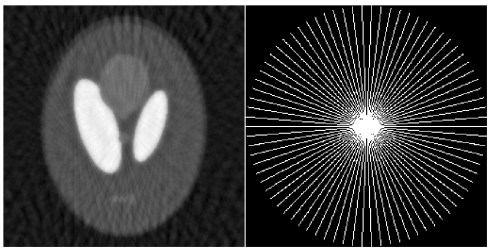

(e) radial AF10

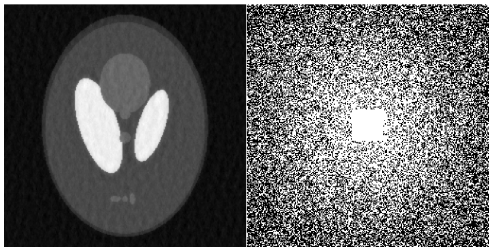

(f) pseudo-random AF2

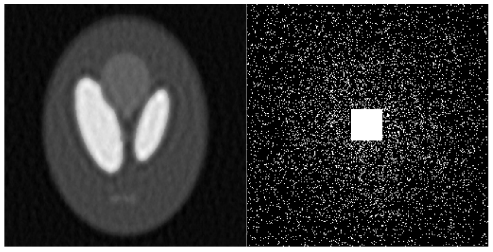

(g) pseudo-random AF10

Figure 2.1: Examples of different undersampling pattern and their influence on image artefacts using standard inverse Fourier transform as reconstruction method.

2.2 Coil-sensitivity estimation, low-resolution images

It is known from parallel imaging that the information of independent receiver coils can be exploited for encoding a part of the spatial information. In order to make use of the information the coil sensitivity profile has to be known. Several algorithms exist to compute coil sensitivity maps from a given number of coil images [[21]-[22]]. Older algorithms [21] solve the problem sequential, first guessing the coil profiles and second reconstructing the image. Newer approaches solve the combined problem by making use of iterative regularized reconstruction methods [22]. Due to the fact that the proposed algorithm incorporates coil sensitivity information it is necessary to compute the coil sensitivity profiles in advance. The algorithm proposed by Ücker et al. [22] is used to compute the coil sensitivity map. The method uses an iterative regularized Gauss-Newton optimization algorithm to solve the problem. Such an optimization method is also used in the present work and described in section 2.5.3. In order to produce low resolution images of the undersampled k-space data, which is necessary for the DESPOT1- initial guess, a block which can be defined in advance, is selected in the center of the k-space. To reduce truncation artifacts associated with the windowing, a Hamming window is used. The low-resolution reconstruction of each receiver channel is combined into one image with the method proposed by Walsh et al. [21]. This image serves as the base for the low-resolution guess.

2.3 B_{1+}-mapping

In order to produce accurate results it is necessary to correct for the imperfect flip angle distribution, both through-plane and in-plane. The through-plane error is reduced by the usage of 3D-image acquisition and neglecting the outermost slices. The in-plane correction needs information about the flip angle distribution across the plane. Several methods exist to measure the flip angle distribution such as the double-angle method [23] which relies

upon intensity differences in magnitude images or the Bloch-Siegert-mapping [24] which uses differences in the phase image to compute the flip angle distribution. The latter method offers the advantage of rapid acquisition and good accuracy even for higher flip angles. Therefore, it is more desirable if short scan time and high precision are required like in parameter mapping which is the case in the present work. The Bloch-Siegert shift occurs if an off-resonant Radio Frequency (RF)-Pulse is applied. The off-resonance RF-Pulse changes the resonance frequency of a nucleus, the amount of shift depends upon $(B_{1+})^2$ and the difference between the spin resonance frequency and the applied RF ω_{RF}. If phase images are acquired, they are in general dependent upon B_0 inhomogeneities, transmit excitation, receive phase, and other sequence-related phase shifts. In order to remove these influences two images at $\pm\omega_{RF}$ are acquired. The difference between those two scans depends up to the first order term solely on the Bloch-Siegert shift and therefore B_{1+} can be calculated, see Equation 2.1. The generated B_{1+} map is used for correcting the flip angle distribution across a slice.

$$\Phi_{BS} = \int_0^T \frac{(\gamma B_{1+}(t))^2}{2\omega_{RF}(t)}\,\mathrm{d}x \tag{2.1}$$

2.4 DESPOT-TV, initial guess

Low resolution images of the k-space center are generated using the method proposed by Walsh et al. [21] and utilized to generate a low resolution initial guess of T_1 and M_0 with the DESPOT1 fitting procedure, proposed by Cheng et al. [7]. The DESPOT1 method is combined with a Total-Variation (TV) regularization and a primal-dual algorithm, proposed by Chambolle and Pock [25], is used to solve the resulting optimization problem. The proposed fitting algorithm equals a pointwise linear regression with a spatial TV regularization in order to suppress noise. The basic form of the DESPOT1 equation [7]

is given by:

$$\underbrace{\frac{S_{FLASH}}{\sin\alpha}}_{d} = \underbrace{E1}_{m}\underbrace{\frac{S_{FLASH}}{\tan\alpha}}_{a_\alpha} + \underbrace{M_0(1-E1)}_{b} \tag{2.2}$$

Rewriting the basic equation into vector-matrix notation, considering the problem has to be solved for every pixel, and introducing the TV-regularization term, leads to the following optimization problem:

$$x^* = \arg\min_x \frac{\lambda}{2}\left\|Ax - d\right\|_2^2 + \frac{1}{2}\left\|\nabla x\right\|_1 \tag{2.3}$$

where:

x : Vector containing the slope m and point of intercept b of the linear equation 2.2

A : System matrix of the linear equation, which can be expressed as a sparse matrix 2.4

d : Defined as in equation 2.2

The vector x is ordered in a way that the slope m is contained in the first half and the intercept b is contained in the second. Therefore the matrix A is composed as in Equation 2.4 where the index refers to the pixel in the image and the whole image is stored in a vector containing all rows concatenated after each other. As shown in Equation 2.4 this matrix is a sparse matrix and therefore can be easily generated and stored in Matlab.

$$A = \begin{pmatrix} a_{\alpha_1 1} & 0 & 0 & 0 & \dots & 1 & 0 & 0 & 0 & \dots \\ a_{\alpha_2 1} & 0 & 0 & 0 & \dots & 1 & 0 & 0 & 0 & \dots \\ \vdots & \vdots & \vdots & \vdots & \vdots & \vdots & \vdots & \vdots & \vdots & \vdots \\ a_{\alpha_n 1} & 0 & 0 & 0 & \dots & 1 & 0 & 0 & 0 & \dots \\ 0 & a_{\alpha_2 1} & 0 & 0 & \dots & 0 & 1 & 0 & 0 & \dots \\ 0 & a_{\alpha_2 2} & 0 & 0 & \dots & 0 & 1 & 0 & 0 & \dots \\ \vdots & \vdots & \vdots & \vdots & \vdots & \vdots & \vdots & \vdots & \vdots & \vdots \end{pmatrix} \tag{2.4}$$

Comparing Equation 2.3 to the standard form of a convex, non-smooth primal problem

in 2.5

$$\min_x F(Kx) + G(x) \tag{2.5}$$

one finds that

$$F(\xi) = \|\xi\|_1 \tag{2.6}$$

$$K = \nabla \tag{2.7}$$

$$G(x) = \frac{\lambda}{2} \|Ax - d\|_2^2 \tag{2.8}$$

and the problem can be written as a general saddle-point problem of the form

$$\begin{aligned} &\min_x \max_y \langle Kx, y\rangle + G(x) - F^*(y) \iff \\ &\min_x \max_y \left\langle x, K^H y\right\rangle + G(x) - F^*(y) \iff \\ &\min_x \max_y - \langle x, \operatorname{div} y\rangle + \frac{\lambda}{2} \|Ax - d\|_2^2 - I_{\|\cdot\|\leq Y}(y) \end{aligned} \tag{2.9}$$

where $I_{\|\cdot\|\leq Y}$ donates the indicator function of Y and Y is the union of pointwise L^2 balls. In order to solve the primal-dual problem one needs the resolvent operators of F^* and G, where F^* denotes the convex conjugate of F. They are defined by (see Chambolle and Pock [25]):

$$\begin{aligned} y &= (I + \sigma \partial F^*)^{-1}(\tilde{y}) = \arg\min_y \left\{ \frac{\|y - \tilde{y}\|_2^2}{2\tau} + F^*(y) \right\} \\ x &= (I + \tau \partial G)^{-1}(\tilde{x}) = \arg\min_x \left\{ \frac{\|x - \tilde{x}\|_2^2}{2\tau} + G(x) \right\} \end{aligned} \tag{2.10}$$

Because F^* is the indicator function the resolvent operator of F^* degenerates to the

pointwise Euclidean projections onto L^2 balls:

$$y = (I + \sigma\partial F^*)^{-1}(\tilde{y}) \iff y_{i,j} = \frac{\tilde{y}_{i,j}}{\max(1, |\tilde{y}_{i,j})|}. \tag{2.11}$$

In order to find the resolvent operator of G one needs to solve a quadratic problem. The solution to this problem is given as:

$$x = (I + \tau\partial G)^{-1}(\tilde{x}) \iff x = \frac{\tilde{x} + \tau\lambda A^T d}{1 + \tau\lambda A^T A} \tag{2.12}$$

Finally, the update steps for the primal-dual algorithm are defined as:

$$\begin{cases} y^{n+1} = (I + \sigma\partial F^*)^{-1}(y^n + \sigma_n K\overline{x}^n) \\ x^{n+1} = (I + \tau\partial G)^{-1}(x^n - \tau_n K^* y^{n+1}) \\ \Theta_n = \frac{1}{\sqrt{1+2\gamma\tau_n}},\ \tau_{n+1} = \Theta_n\tau_n,\ \sigma_{n+1} = \frac{\sigma_n}{\Theta_n} \\ \overline{x}^{n+1} = x^{n+1} + \theta(x^{n+1} - x^n) \end{cases} \tag{2.13}$$

The initial step sizes are chosen such as

$$\sigma\tau < L \tag{2.14}$$

holds true. The Lipschitz constant L of the linear operator K, the gradient operator, is known to be 8. Therefore, $\sigma = \tau = \frac{1}{\sqrt{8}}$ are chosen as the initial step size. If the optimal $x^\star$ is found, one can calculate T_1 and M_0 through

$$T_1 = \frac{-T_R}{\ln(m)} \tag{2.15}$$

$$M_0 = \frac{b}{1 - m} \tag{2.16}$$

where:

m : is the slope of the linear equation

b : is the intersection with the y-axis

The whole process of linear regression with spatial TV constrained is illustrated in Figure 2.4.

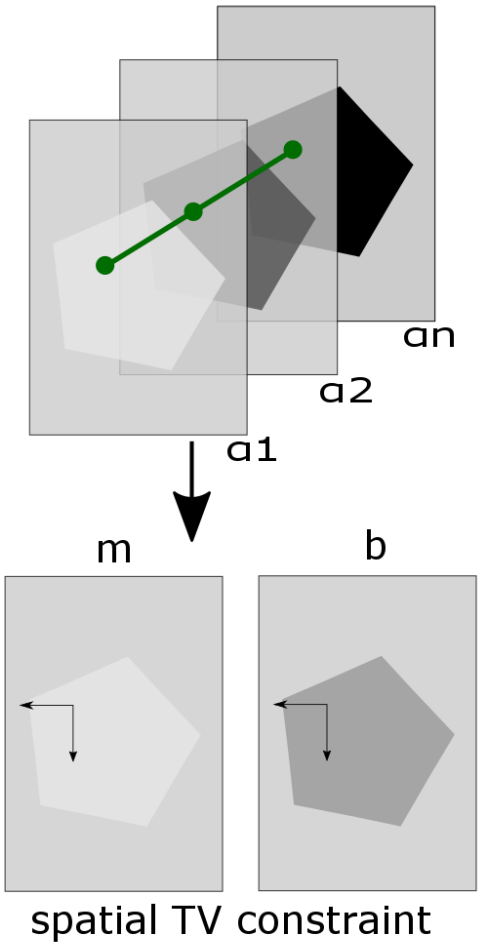

Figure 2.2: Graphical schematic of the initial-guess algorithm. The upper part of the figure shows the pixel wise linear regression along the different flip angles. Subsequent a spatial TV constrained is applied to smooth the result. The TV constraint is represented as the two vectors in the lower part of the image.

2.5 Model-based Reconstruction

Model-based reconstruction combines the signal equation and additional a-priori information, like coil sensitivity and knowledge about the undersampling pattern, to generate a model of the MRI signal in every pixel. The base of this work is the steady-state signal equation of the FLASH-sequence 2.17 which depends on T_1 and M_0. The T_2^* influence is neglected.

$$S\left(M_0, T_1, \alpha\right) = M_0 \sin\alpha \frac{1 - e^{-\frac{T_R}{T_1}}}{1 - e^{-\frac{T_R}{T_1}} \cos\alpha} \tag{2.17}$$

Where:

$$\begin{aligned} M_0 &: \text{unknown } M_0\text{-map} \in \mathbb{R}_+^{n\times m} \quad &: n,\, m \in \mathbb{N}_+ \\ T_1 &: \text{unknown } T_1\text{-map} \in \mathbb{R}_+^{n\times m} \quad &: n,\, m \in \mathbb{N}_+ \\ \alpha &: \text{known flip-angle} \in [-\pi, \pi] \end{aligned}$$

In order to use the proposed optimization algorithms, one needs the derivatives with respect to T_1 and M_0 of the signal equation 2.17 which are given by 2.18and 2.19.

$$\frac{\partial S}{\partial M_0} = \sin\alpha \frac{1 - e^{-\frac{-T_R}{T_1}}}{1 - e^{-\frac{T_R}{T_1}} \cos\alpha} \tag{2.18}$$

$$\frac{\partial S}{\partial T_1} = -\frac{M_0 T_R e^{\frac{T_R}{T_1}} \left(2\sin\alpha - 2\cos\alpha\sin\alpha\right)}{2T_1^2 \left(e^{\frac{T_R}{T_1}} - \cos\alpha\right)^2} \tag{2.19}$$

Casting the problem of finding M_0 and T_1 into the form of a basic minimization problem, minimizing the difference between the model generated data and the measured data by the means of a L_2 norm, yields:

$$\min_x \frac{1}{2} \|G(x) - d\|_2^2 + \mathcal{R}(x) \tag{2.20}$$

Where:

$$\begin{aligned} x &: \text{Vector of } M_0,\, T_1 \in \mathbb{R}_+^{2\times n\times m} \\ d &: \text{Measured data} \in \mathbb{C}^{n\times m\times i\times k} \\ G &: X \to Y \\ R &: \text{Some regularization term} \end{aligned}$$

The operator G contains the whole signal model, coil sensitivity information, the Fourier transform, and the undersampling pattern. This process is described by Equation 2.21.

$$G : x \to \begin{pmatrix} P_k \mathcal{F}\left[C_i S\left(M_0, T_1, \alpha_k\right)\right] \\ \vdots \end{pmatrix} \tag{2.21}$$

Where:

$$\begin{aligned} k = 1 \ldots M &: \text{Number of flip angles} \\ i = 1 \ldots N &: \text{Number of coils} \\ P_k &: \text{Undersampling pattern} \\ C_i &: \text{Coil sensitivity} \end{aligned}$$

Checking the convexity of the function using the “convexchecker“ tool provided by Bapi Chatterjee at Indian Institute of Technology Delhi, New Delhi, India, it can be shown that the function is not globally convex nor linear. Therefore nonlinear solvers have to be used to find the minimum and thus the desired values of T_1 and M_0. The non convexity of the function is a major problem because there exists no necessary optimality condition for non convex functions. Therefore no algorithm is provably able to guarantee convergence to the global solution. Different algorithms exist to solve non-linear problems but no mathematical proof can be given, that the solution is truly the global minimum. They can be divided into two major categories namely first order methods which make use of the gradient information to solve the problem, the Conjugate Gradient (CG)-algorithm belongs to this group, and second order methods which use additional information from

the Hessian matrix. Computing the Hessian can be very demanding and for larger problems storing the matrix is not possible. Therefore, methods exist which approximate the Hessian in every iteration. The IRGN-algorithm which linearizes the problem in every step and solves the linearized problem afterwards is such an algorithm. Both methods, CG and IRGN, are implemented and described in detail in the following sections.

2.5.1 Parameter and data scaling

An important part in solving the problem at hand is the scaling of the parameters and the data. The parameter scaling is done by dividing every pixel by the maximum of the value of interest, found in the initial guess. This generates maps in the range of [0,1]. Using the described scaling is crucial for the optimization algorithms because the parameters are separated by several orders which results in a not converging algorithm if not scaled appropriate. Scaling of the data is used to make the problem at hand independent of the actual measurement. This is important because the data is dependent on the actual SNR and other sequence related entities which are only relative for MRI. This dependency would give rise to the problem of choosing between the weight of data and the regularization term dependent on the measurement. Scaling the data enables the use of a fixed regularization parameter, thus providing a robust algorithm for various experiments.

2.5.2 CG_descent

CG_descent, developed by William Hager, University of Florida, Department of Mathematics, is a collection of CG-methods using different line-search algorithms and gradient information up to incorporating information of a (quasi)-Hessian matrix, the LBFGS approach. The collection features a C-implementation as well as a Matlab MEX-file implementation of the algorithms. The two optimization algorithms used in the present

work are explained in detail on the following pages. For further information regarding the CG_descent script and possible usages the interested reader is referred to [26][27].

2.5.2.1 Conjugate Gradient

Conjugate gradient methods are widely used in optimization problems because of their fast convergence speed and low memory requirement. They are not only suitable for linear problems but also for nonlinear problems and their convergence behavior for linear problems is well studied [27]. Even though there exists no convergence proof for nonlinear problems they perform rather well in practice on such types of problems. First order methods require a continuously differentiable cost function and thus are restricted to smooth regularization methods. This limits their potential to reproduce sharp edges which leads to a blurred image. To solve a problem the CG-algorithm is initialized with an initial guess $x_0 \in \mathcal{R}^n$ and generates a sequence x_k, $k \geq 1$ by using the recurrence:

$$x_{k+1} = x_k + \alpha_k d_k \tag{2.22}$$

Where α_k is the step size obtained by a line search and d_k the direction generated by

$$d_{k+1} = -g_{k+1} + \beta_k d_k, \;\; d_0 = -g_0 \tag{2.23}$$

where β_k is the CG update parameter which has a strong influence on convergence of the algorithm and $g_k = \nabla f(x_k)^T$, the gradient of f at x_k. Hager et al. suggest to use the update scheme in Equation 2.24 for optimal performance which is also implemented in their algorithm. For detailed explanation of the proposed update scheme, the reader is referred to [28].

$$\beta_k = \left(y_k - 2d_k \frac{\|y_k\|_2^2}{d_k^T y_k} \right)^T \frac{g_{k+1}}{d_k^T y_k} \tag{2.24}$$

Another important part in a CG algorithm is the line search which has to ensure that a sufficient descent is achieved and has significant impact on convergence and stability of the

overall algorithm. The ideal point to terminate the line search is reached if the standard Wolfe conditions are fulfilled. However, the proposed algorithm performs better if the stronger approximate Wolfe conditions are fulfilled which where introduced by Hager et al [28]. Furthermore the standard Wolfe conditions limit the precision of the algorithm to the order of the square root of the machine precision. By using the approximate Wolfe conditions the precision can be increased to the order of machine precision. The approximate Wolfe conditions are given by:

$$\sigma g_k^T d_k \leq g_{k+1}^T d_k \leq (2\delta - 1) g_k^T d_k \tag{2.25}$$

Where $0 < \delta < \frac{1}{2}$ and $\delta < \sigma < 1$. Even though there is no convergence theory for the approximate Wolfe conditions in CG algorithms they yield a practical performance much better than that of the standard or generalized or strong Wolfe conditions [27].

2.5.2.2 LBFGS

LBFGS belongs to the quasi-Newton methods which approximate the Hessian matrix. In contrast to Broyden-Fletcher-Goldfarb-Shanno (BFGS) which uses all previous iterations to approximate the Hessian in every step, the limited memory approach uses only the last m iterations to calculate the Hessian. This is especially useful when dealing with large scale problems like in the present work. Similar to the CG methods they require a continuously differentiable cost function and thus are limited to smooth regularization methods. Because of the approximation of the Hessian with first order derivatives they can deal with function which are only one-time differentiable.

The general start of a BFGS method is defining a positive semi-definit matrix H_0 (often identity), $s_k = x_{k+1} - x_k$ and $y_k = \nabla f(x_{k+1}) - \nabla f(x_k)$. The update formula for the

approximate Hessian H written in product form is given by

$$H_{k+1} = \left(I - \rho y s^T\right) H_k \left(I - \rho y s^T\right) + \rho s s^T \equiv v^t H_k v + \rho s s^T \tag{2.26}$$

where $\rho = \frac{1}{y^T s}$. Using this formula it is easy to implement an limited-memory BFGS-algorithm assuming $v = I$ and $\rho s s^T = 0$ is equivalent to dropping a correction term. As an example the number of corrections stored m = 2:

$$H_0 = I \tag{2.27}$$

$$H_1 = v_0^T H_0 v_0 + \rho_0 s_0 s_0^T \tag{2.28}$$

$$H_2 = v_1^T v_0^T H_0 v_0 v_1 + v_1^T \rho_0 s_0 s_0^T v_1 + \rho_1 s_1 s_1^T \tag{2.29}$$

Updating to H_3 needs to drop the oldest infromation:

$$H_3 = v_2^T v_1^T H_1 v_1 v_2 + v_2^T \rho_1 s_1 s_1^T v_2 + \rho_2 s_2 s_2^T \tag{2.30}$$

$$\vdots$$

The update for x_k is obtained by a linesearch similar to the gradient method

$$x_{k+1} = x_k + \alpha_k p_k \tag{2.31}$$

where α_k is the step size obtained by the line search and p_k is the direction obtained by:

$$p_k = -H_k \nabla f(x_k) \tag{2.32}$$

The present work uses the same linesearch as the CG implementation because it was shown by Hager et al. [26] that this particular implementation performed best. For detailed information about the LBFGS method the interested reader is referred to [29].

2.5.3 IRGN-TGV

IRGN-methods linearize the problem with a Taylor-series expansion truncated after the first order term in every Gauss-Newton-step and solve the linear problem afterwards. The fact that they only need the derivative of the model rather than the derivatives of the whole cost function enables the use of L_1 based regularization methods. A regularization term which allows sharp edges and smooth structures in images is the TGV-term [30]. TGV best reflects the properties of a parameter map (sharp edges at tissue boundaries, smooth within the tissue) and is therefore used as regularization term in this work. An effective method for solving a TGV problem is the primal-dual approach, introduced by Chambolle and Pock [25] which is described below.

The problem of finding M_0 and T_1 in Equation 2.17 is a non-linear problem and we use a Taylor-series expansion truncated after the first order term to linearize the MRI signal model:

$$G(x) \approx G(x_j) + \underbrace{\frac{\partial G}{\partial x}|_{x=x_j}}_{\mathrm{DG}}(x - x_j) \tag{2.33}$$

The derivative of G at the expansion point with respect to the parameters is called DG. DG maps the changes of the parameters $x - x_j$ which lie in parameter space to the data space. DG can be calculated as:

$$DG : x - x_j = \begin{pmatrix} M_0 - M_{0j} \\ T_1 - T_{1j} \end{pmatrix} \rightarrow \left(P_k \mathcal{F} \left[C_i \left. \frac{\partial S(\alpha_k)}{\partial M_0} \right|_{M_0 = M_{0j}, T_1 = T_{1j}} (M_0 - M_{0j}) \right] + P_k \mathcal{F} \left[C_i \left. \frac{\partial S(\alpha_k)}{\partial T_1} \right|_{M_0 = M_{0j}, T_1 = T_{1j}} (T_1 - T_{1j}) \right] \right) = y \tag{2.34}$$

In order to solve the linear problem one needs to calculate the adjoint to DG which is shown in 2.35.

$$DG^H : y \rightarrow \begin{pmatrix} \sum_{k=1}^{\#\alpha} \left. \overline{\frac{\partial S(\alpha_k)}{\partial M_0}} \right|_{M_0 = M_{0j}, T_1 = T_{1j}} \sum_{i=1}^{\#\text{coils}} \overline{C_i} \mathcal{F}^{-1} P_k y \\ \\ \sum_{k=1}^{\#\alpha} \left. \overline{\frac{\partial S(\alpha_k)}{\partial T_1}} \right|_{M_0 = M_{0j}, T_1 = T_{1j}} \sum_{i=1}^{\#\text{coils}} \overline{C_i} \mathcal{F}^{-1} P_k y \end{pmatrix} \tag{2.35}$$

In each linearization step (Gauss-Newton-Step) the following TGV regularized problem has to be solved:

$$
\begin{aligned}
x^{\star}_{j+1} =& \arg\min_{x} \frac{\lambda}{2} \left\| DG(x) - \tilde{d} \right\|_2^2 + \mathrm{TGV}(x) + \frac{1}{2\delta} \left\| x - x_j \right\| = \\
& \arg\min_{\substack{M_0, T_1, \\ v_o, v_1}} \alpha_1 \|\nabla M_0 - v_o\|_1 + \alpha_0 \|\varepsilon(v_o)\|_1 + \beta_1 \|\nabla T_1 - v_1\|_1 + \beta_0 \|\varepsilon(v_1)\|_1 \\
& + \frac{\lambda}{2} \left\| DG|_{M_0 = M_{0j}, T_1 = T_{1j}} \begin{pmatrix} M_0 \\ T_1 \end{pmatrix} - \underbrace{\left(d - G\begin{pmatrix} M_{0j} \\ T_{1j} \end{pmatrix} + DG|_{M_0 = M_{0j}, T_1 = T_{1j}} \begin{pmatrix} M_{0j} \\ T_{1j} \end{pmatrix} \right)}_{\text{residuum } \tilde{d}} \right\|_2^2 \\
& + \frac{1}{2\delta} \left\| \begin{pmatrix} M_0 - M_{0j} \\ T_1 - T_{1j} \\ 0 \\ 0 \end{pmatrix} \right\|_2^2
\end{aligned}
\tag{2.36}
$$

To solve this problem efficiently one may use the primal-dual algorithm. In order to use this algorithm the problem at hand has to be compared to the standard form of the primal minimization problem

$$
\min_{x} F(Kx) + G(x) \tag{2.37}
$$

where F and G are convex functions and K is a continuous linear operator. Comparing this formulation with our problem in 2.36 to identify F, G, and K leads to:

$$
\begin{aligned}
F(y) &= \underbrace{\alpha_1\|z_1\|_1 + \alpha_0\|z_2\|_1 + \beta_1\|z_3\|_1 + \beta_0\|z_4\|_1}_{\text{dualization of the parameters}} + \underbrace{\frac{\lambda}{2}\|r\|_2^2}_{\text{dualization of the data term}} \\
G(\xi) &= \frac{1}{2\delta}\left\|\begin{pmatrix} \xi_1 - M_{0j} \\ \xi_2 - T_{1j} \\ 0 \\ 0 \end{pmatrix}\right\|_2^2 \\
K(x) &= \begin{pmatrix} \nabla & 0 & -\mathrm{Id} & 0 \\ 0 & 0 & \varepsilon & 0 \\ 0 & \nabla & 0 & -\mathrm{Id} \\ 0 & 0 & 0 & \varepsilon \\ DG_1 & DG_2 & 0 & 0 \end{pmatrix} \underbrace{\begin{pmatrix} M_0 \\ T_1 \\ v_0 \\ v_1 \end{pmatrix}}_{x} \\
K^T(y) &= \begin{pmatrix} -div_1 & 0 & 0 & 0 & DG_1^H \\ 0 & 0 & -div_1 & 0 & DG_2^H \\ -Id & -div_2 & 0 & 0 & 0 \\ 0 & 0 & -Id & -div_2 & 0 \end{pmatrix} \underbrace{\begin{pmatrix} z_1 \\ z_2 \\ z_3 \\ z_4 \\ r \end{pmatrix}}_{y}
\end{aligned}
\tag{2.38}
$$

The primal-dual algorithm needs the resolvent operators of F^* and G, where F^* denotes the convex conjugate of F. The resolvent operator of F^* is defined as:

$$
\begin{aligned}
x = (I + \sigma\partial F^*)^{-1}(y) &= \arg\min_x \left\{ \frac{\|x-y\|_2^2}{2\sigma} + F^*(x) \right\} \\
F^*(y) &= I_{\|\cdot\|\leq\alpha_1}(z_1) + I_{\|\cdot\|\leq\alpha_0}(z_2) + I_{\|\cdot\|\leq\beta_1}(z_3) + I_{\|\cdot\|\leq\beta_0}(z_4) + \frac{1}{2\lambda}\|r\|_2^2 \\
\Rightarrow (I + \sigma\partial F^*)^{-1}(y) &= \underbrace{\frac{y_i}{\max\left(1, \frac{|y_i|}{\alpha_i,\beta_i}\right)}}_{P_i:\ i=1\ldots4}, \underbrace{\frac{r}{1+\frac{\sigma}{\lambda}}}_{P_{L^2}}
\end{aligned}
\tag{2.39}
$$

The resolvent operator of G is defined as:

$$
\begin{aligned}
x = (I + \sigma\partial G)^{-1}(y) &= \arg\min_x \left\{ \frac{\|x-y\|_2^2}{2\sigma} + G(x) \right\} \Rightarrow \\
(I + \sigma\partial G)^{-1}(y) &= \begin{pmatrix} \underbrace{\frac{\tau\delta M_{0j} + y_1}{1+\tau\delta}}_{P_{M_0}} \\ \underbrace{\frac{\tau\delta T_{1j} + y_2}{1+\tau\delta}}_{P_{T_1}} \\ Id \\ Id \end{pmatrix}
\end{aligned}
\tag{2.40}
$$

The resolvent operator of G is only used on M_0 and T_1 because $G \equiv 0$ for v_0 and v_1. Therefore, the resolvent operator for v_0 and v_1 becomes simply identity. The general update steps of the primal-dual algorithm are defined as

$$
\begin{aligned}
y^{n+1} &= (I + \sigma\partial F^*)^{-1}(y^n + \sigma K\overline{x}^n) \\
x^{n+1} &= (I + \tau\partial G)^{-1}(x^n - \tau K^T y^{n+1}) \\
\overline{x}^{n+1} &= x^{n+1} + \theta(x^{n+1} - x^n)
\end{aligned}
\tag{2.41}
$$

where $\theta = 1$ is chosen for the extrapolation step as proposed by Chambolle and Pock [25]. In order to promote convergence we introduce an adaptive step size, as proposed by Bredies et al. [31], which is computed after each iteration. Given $\Theta \in (0, 1)$ and $\eta > 0$, after each iteration we update σ and τ, e.g. $\eta = 1$ equal step sizes for primal and dual, as

$$\begin{aligned} \sigma &= \mathcal{S}\left(\sigma\tau, \frac{\|x^{n+1} - x^n\|_X}{\|K(x^{n+1} - x^n)\|_Y}\right)\eta \\ \tau &= \mathcal{S}\left(\sigma\tau, \frac{\|x^{n+1} - x^n\|_X}{\|K(x^{n+1} - x^n)\|_Y}\right)/\eta \end{aligned} \tag{2.42}$$

where

$$S(\sigma\tau, \xi) = \begin{cases} \xi & if\ \sqrt{\Theta\sigma\tau} \geq \xi, \\ \sqrt{\Theta\sigma\tau} & if\ \sqrt{\sigma\tau} \geq \xi\sqrt{\Theta\sigma\tau},) \\ \sqrt{\sigma\tau} & else \end{cases} \tag{2.43}$$

The initial step sizes are chosen such as

$$\sigma\tau < L \tag{2.44}$$

holds true. The Lipschitz constant L of the linear operator K is approximated in every IRGN iteration through power-iteration.

The problem of finding the optimal value for x in every Gauss-Newton step can be described by the following pseudo-code:

Initialize: (M_0, T_1, v_0, v_1), $(\overline{M_0}, \overline{T_1}, \overline{v_0}, \overline{v_1})$, (z_1, z_2, z_3, z_4), $\sigma, \tau > 0$, $\eta = \theta = 1$

Iterate:

Dual Update:

$z_1^{n+1} \leftarrow P_1\left(z_1^n + \sigma(\nabla\overline{M_0} - \overline{v_0})\right)$

$z_2^{n+1} \leftarrow P_2\left(z_2^n + \sigma\epsilon(\overline{v_0})\right)$

$z_3^{n+1} \leftarrow P_3\left(z_3^n + \sigma(\nabla\overline{T_1} - \overline{v_1})\right)$

$z_4^{n+1} \leftarrow P_4\left(z_4^n + \sigma\epsilon(\overline{v_1})\right)$

$r^{n+1} \leftarrow P_{L^2}\left(r^n + \sigma(DG(\frac{\overline{M_0}}{\overline{T_1}}) - \tilde{d})\right)$

Primal Update:

$M_0^{n+1} \leftarrow P_{M_0}\left(M_0^n - \tau\left(-div_1 z_1^{n+1} + DG_1^H(r^{n+1})\right)\right)$

$T_1^{n+1} \leftarrow P_{T_1}\left(T_1^n - \tau\left(-div_1 z_3^{n+1} + DG_2^H(r^{n+1})\right)\right)$

$v_0^{n+1} \leftarrow v_0 - \tau\left(-div_2 z_2^{n+1} - z_1^{n+1}\right)$

$v_1^{n+1} \leftarrow v_1 - \tau\left(-div_2 z_4^{n+1} - z_3^{n+1}\right)$

Stepsize Update:

$\sigma_{n+1} \leftarrow \mathcal{S}\left(\sigma\tau, \frac{\|x^{n+1}-x^n\|}{\|K(x^{n+1}-x^n)\|}\right)$

$\tau_{n+1} \leftarrow \sigma_{n+1}$

Extrapolation and update:

$(\overline{M_0}, \overline{T_1}, \overline{v_0}, \overline{v_1}) \leftarrow 2(M_0^{n+1}, T_1^{n+1}, v_0^{n+1}, v_1^{n+1}) - (M_0^n, T_1^n, v_0^n, v_1^n)$

$(M_0^n, T_1^n, v_0^n, v_1^n) \leftarrow (M_0^{n+1}, T_1^{n+1}, v_0^{n+1}, v_1^{n+1})$

Algorithm 1: Primal-dual algorithm for solving the TGV regularized model-based reconstruction of VFA data in every Gauss-Newton step.

3 Results

3.1 Numerical simulations

3.1.1 Phantom generation

The numerical simulations are performed with the "Modified Shepp-Logan phantom" from Matlab, the Mathworks Inc., see Figure 3.1. In order to simulate realistic T_1 times we set the T_1 time constant of the different regions to the values listed in Table 3.1. Furthermore, we simulate four different receiver coils, which are located at the corner of the image. The sensitivities are simulated with the Biot-Savart law and the Matlab script provided by Matthie Guerquin-Kern [32]. The simulated T_1 map along with simulated coil sensitivities, are plugged into the signal equation for the FLASH sequence 1.16 to generate magnitude images. We simulate three different flip angles, 3°, 10° 16°, and modulate a phase onto the coil sensitivities to take phase effects of in vivo imaging into account, see Figure 3.3. All images are generated with TR/TE = 3.4ms/1.1ms and a matrix size of 256x256 pixel. Furthermore, we also take T_2 effects into account by adding the term $e^{-\frac{TE}{T_2}}$ multiplicative to the signal equation. All images have an additive common noise term and a random additive coil noise term, which is generated separately for every coil, leading to an SNR of 20 or worse depending on the position, as can be seen in Figure 3.2. The last step is a 2D-Fourier transform to generate k-space data.

Table 3.1: T_1 and M_0 reference values of the numerical Shepp-Logan phantom.

Region	T_1 in ms	M_0 in a.u.
1	3000	4
2	1200	1.5
3	800	2
4	500	2

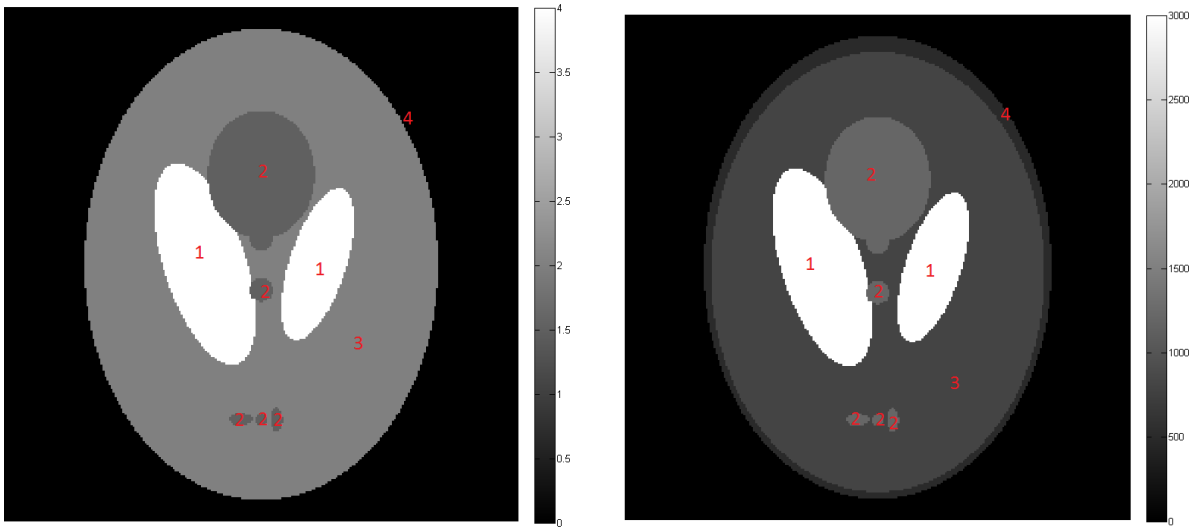

(a) Reference M_0

(b) Reference T_1

Figure 3.1: Reference parameter maps for T_1 and M_0 of the numerical Shepp-Logan phantom.

3.1.2 Numerical results of CG_descent

All results were generated with the default parameters for the CG_descent algorithm using the modifications shown in Table 3.2. Memory denotes the number of gradient vectors stored in order to approximate the Hessian matrix.

Table 3.2: CG_descent and LBFGS parameter set for numerical phantoms.

CG restarts	LBFGS	CG maxit	memory
10	true	100	5

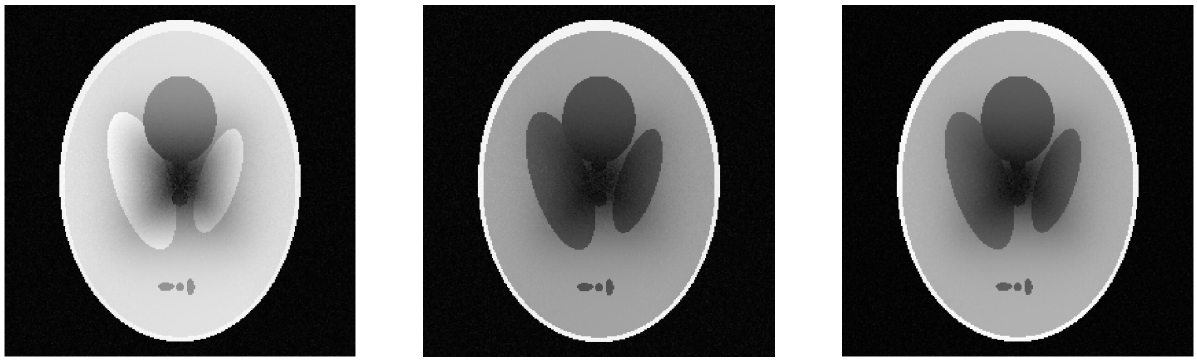

(a) Simulated magnitude image for $\alpha = 3°$

(b) Simulated magnitude image for $\alpha = 16°$

(c) Simulated magnitude image for $\alpha = 10°$

Figure 3.2: Numerically simulated magnitude images for different flip angles.

Interleaved pattern

The results for an interleaved undersampling pattern are shown in Figure 3.4. The image in the upper left corner of the figure shows the reference T_1 map used. To the right of the reference is a fully sampled reconstruction generated with the CG_descent algorithm and further to the right are the results for increased undersampling, namely 6 and 12 fold acceleration. The difference between the reference image and the accelerated reconstruction are illustrated below the corresponding parameter map and are given in percent. The mean and standard deviation for the different ROIs shown in Figure 3.4 were evaluated with Matlab and are presented in Table 3.3. Additionally the results were evaluated along a line horizontally and vertically through the center of the image. The results of this evaluation are shown in Figure 3.5. The computation time for one reconstruction was approximately 20 minutes on a 64 Bit Windows 7 PC with an Intel Core i5-3350p @ 3.10 GHz with 16 GB of RAM.

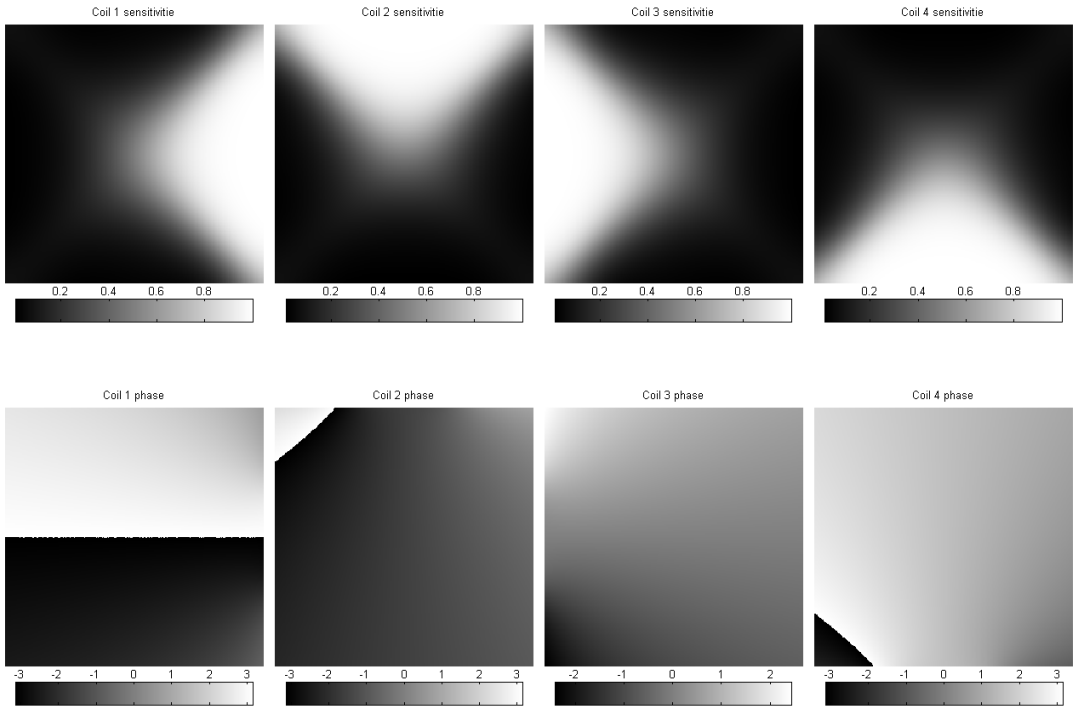

Figure 3.3: Simulated coil sensitivities and phase for the four receiver coils.

3.1.3 Numerical results IRGN

All results were generated with the parameters for the IRGN-TGV algorithm shown in Table 3.4.

Interleaved pattern

The results for an interleaved undersampling pattern are shown in Figure 3.6. The image in the upper left corner of the figure shows the reference T_1 map used. To the right are the results of the IRGN-TGV algorithm for increasing acceleration, starting at 1 (no acceleration) to 6 and finally 12 fold acceleration. The difference between the reference image and the accelerated reconstruction are illustrated below the corresponding parameter map and are given in percent. The mean and standard deviation for the different

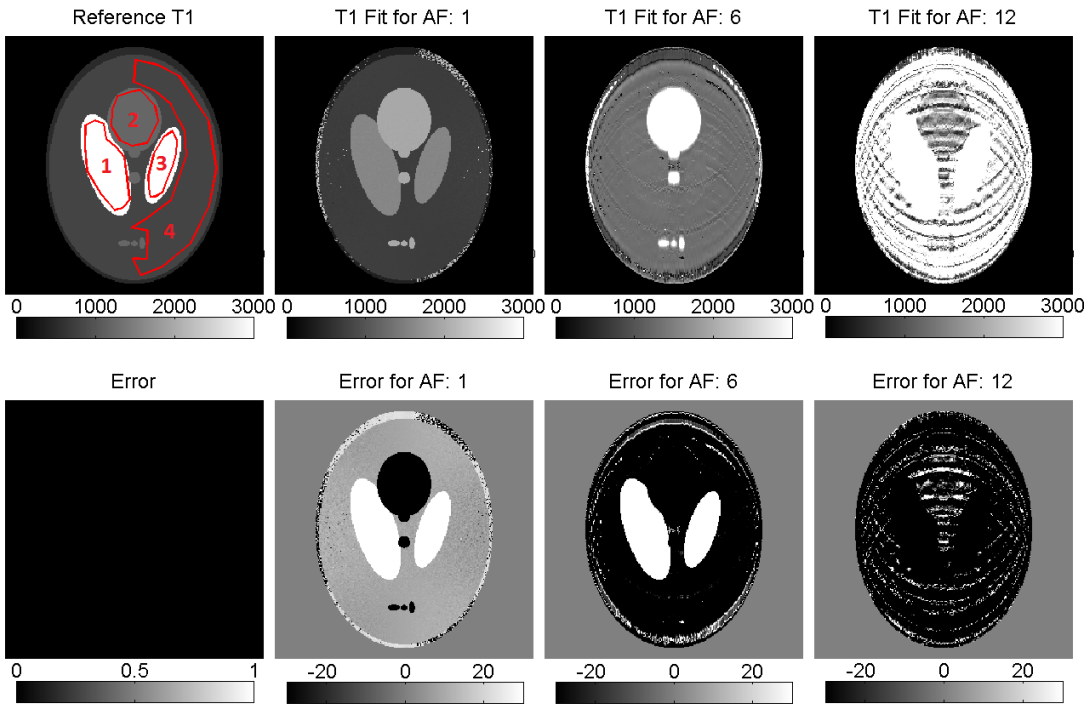

Figure 3.4: Estimated parameter maps of T_1 from the CG_descent algorithm with an interleaved undersampling scheme and the corresponding fitting error in percent for different acceleration factors.

ROIs shown in Figure 3.6 were evaluated and are presented in Table 3.5. Additionally the results were evaluated along a line horizontally and vertically through the center of the image. The results of this evaluation are shown in Figure 3.7. The computation time for one reconstruction was approximately 8 hours on a 64 Bit Windows 7 PC with an Intel Core i5-3350p @ 3.10 GHz with 16 GB of RAM.

Radial pattern

The results for a radial undersampling pattern are shown in Figure 3.8. The image in the upper left corner of the figure shows the reference T_1 map used. To the right are the results of the IRGN-TGV algorithm for increasing acceleration, starting at 1 (no acceleration) to 6 and finally 12 fold acceleration. The difference between the reference

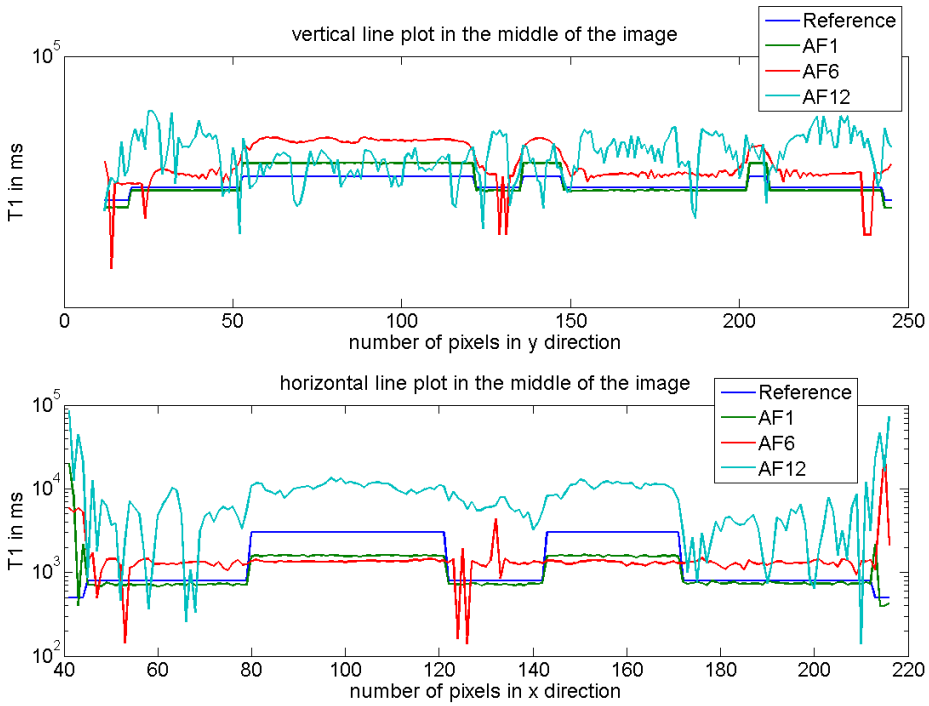

Figure 3.5: Line profile along the x- and y-axis of the resulting T_1 fit using an interleaved undersampling scheme for different acceleration factors and the CG_descent algorithm. The center of the image is assumed to be the origin of the coordinate system.

image and the accelerated reconstruction are shown below the corresponding parameter map and are given in percent. The mean and standard deviation for the different ROIs shown in Figure 3.8 were evaluated and are presented in Table 3.6. Additionally the results were evaluated along a line horizontally and vertically through the center of the image. The results of this evaluation are shown in Figure 3.9. The computation time for one reconstruction was approximately 8 hours on a 64 Bit Windows 7 PC with a Intel Core i5-3350p @ 3.10 GHz with 16 GB of RAM.

Table 3.3: Mean and SD of the different ROIs and acceleration factors of the numerical phantom using an interleaved undersampling scheme and a CG_descent optimization algorithm. ROIs are defined as in Figure 3.4

	Reference T_1 mean in ms	Reference T_1 SD in ms	ACC 1 mean T_1 in ms	ACC 1 SD T_1 in ms
Roi 1	3000.000	0.000	1582.151	19.969
Roi 2	1200.000	0.000	1978.329	12.312
Roi 3	3000.000	0.000	1576.826	21.883
Roi 4	800.000	0.000	739.010	589.248
	ACC 6 mean T_1 in ms	ACC 6 SD T_1 in ms	ACC 12 mean T_1 in ms	ACC 12 SD T_1 in ms
Roi 1	1345.141	103.592	10610.254	1562.141
Roi 2	4590.451	279.942	1865.925	781.107
Roi 3	1346.864	98.272	10179.205	1478.765
Roi 4	1298.655	196.410	4307.804	2624.727

Table 3.4: IRGN-TGV parameter set for numerical phantoms.

initial TGV iterations	maximal TGV iterations	IRGN iterations	
1	1000	100	
λ	δ	σ	τ
$1.6e^4$	10	$\frac{1}{\sqrt{4\sqrt{2}+16+L}}$	$\frac{1}{\sqrt{4\sqrt{2}+16+L}}$
α_0	α_1	β_0	β_1
1	$\sqrt{2}$	1	$\sqrt{2}$

Pseudo random pattern

The results for a pseudo random undersampling pattern are shown in Figure 3.10. The image in the upper left corner of the figure shows the reference T_1 map used. To the right are the results of the IRGN-TGV algorithm for increasing acceleration, starting at 1 (no acceleration) to 6 and finally 12 fold acceleration. The difference between the reference image and the accelerated reconstruction are illustrated below the corresponding parameter map and are given in percent. The mean and standard deviation for the different ROIs shown in Figure 3.10 were evaluated and are presented in Table 3.7. Additionally the results were evaluated along a line horizontally and vertically through the center of the image. The results of this evaluation are shown in Figure 3.11. The computation time for one reconstruction was approximately 8 hours on a 64 Bit Windows 7 PC with a Intel

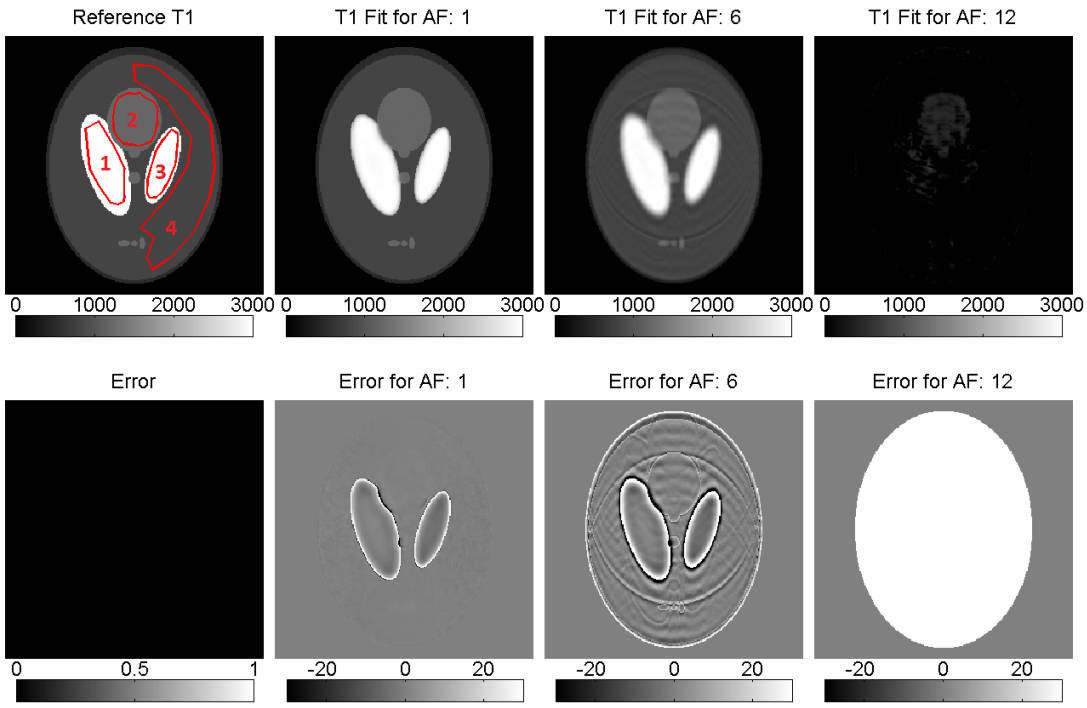

Figure 3.6: Estimated parameter maps of T_1 from the IRGN-TGV algorithm with an interleaved undersampling scheme and the corresponding fitting error in percent for different acceleration factors.

Core i5-3350p @ 3.10 GHz with 16 GB of RAM.

3.1.4 Influence of the B_{1+} map

In order to show the influence of errors in the B_{1+} map, a simulated B_{1+} field map as shown in Figure 3.12 was modulated onto the numerical phantom. The phantom size was 128x128 pixel with the same properties for T_1 and M_0 as in Figure 3.1(b) and 3.1(a). The results for no B_{1+} correction, 1% error and 5% error in the B_{1+} map are shown in Figure 3.13. Furthermore, a line plot along the x- respectively y-Axis is shown in Figure 3.14 and the mean and standard deviation for different ROIs is calculated and presented in Table 3.8. All reconstructions were performed using no acceleration to better demonstrate the influence of B_{1+} errors. Reconstruction time for this lower resolution was

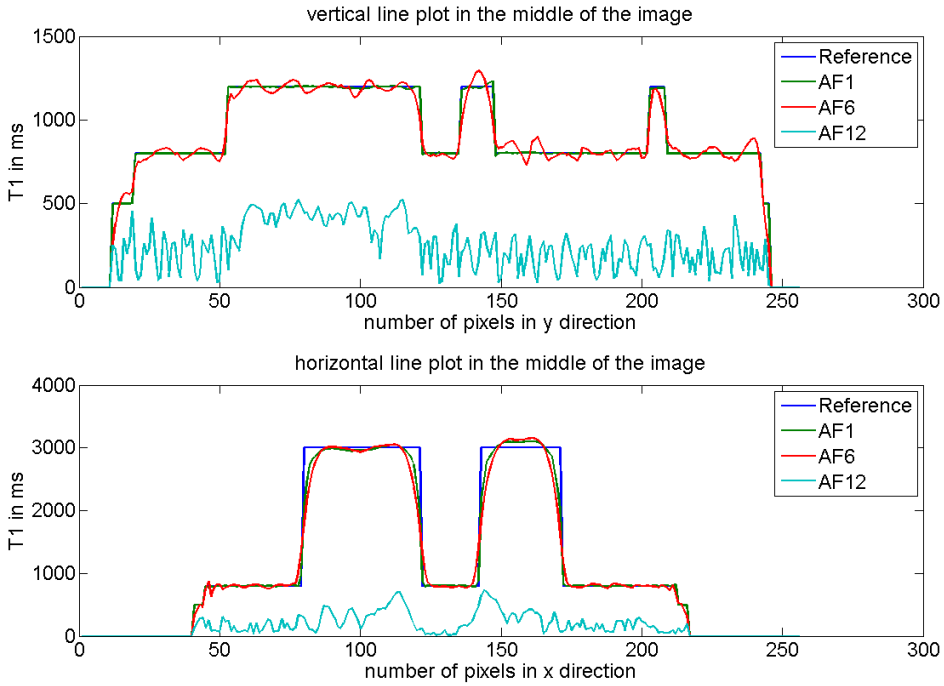

Figure 3.7: Line profile along the x- and y-axis of the resulting T_1 fit using an interleaved undersampling scheme for different acceleration factors and the IRGN-TGV algorithm. The center of the image is assumed to be the origin of the coordinate system.

2 hours on a 64 Bit Windows 7 PC with an Intel Core i5-3350p @ 3.10 GHz with 16 GB of RAM.

Table 3.5: Mean and SD of the different ROIs and acceleration factors with an interleaved undersampling scheme of the numerical phantom and the IRGN-TGV algorithm. ROIs are defined as in Figure 3.6

	Reference T_1 mean in ms	Reference T_1 SD in ms	ACC 1 mean T_1 in ms	ACC 1 SD T_1 in ms
Roi 1	3000.000	0.000	2997.053	51.635
Roi 2	1200.000	0.000	1195.197	5.289
Roi 3	3000.000	0.000	3033.521	99.151
Roi 4	800.000	0.000	800.129	4.439
	ACC 6 mean T_1 in ms	ACC 6 SD T_1 in ms	ACC 12 mean T_1 in ms	ACC 12 SD T_1 in ms
Roi 1	3001.475	94.445	-38.467	263.285
Roi 2	1194.539	35.206	346.940	130.178
Roi 3	2988.765	211.739	-156.633	226.196
Roi 4	800.080	31.798	-150.576	101.199

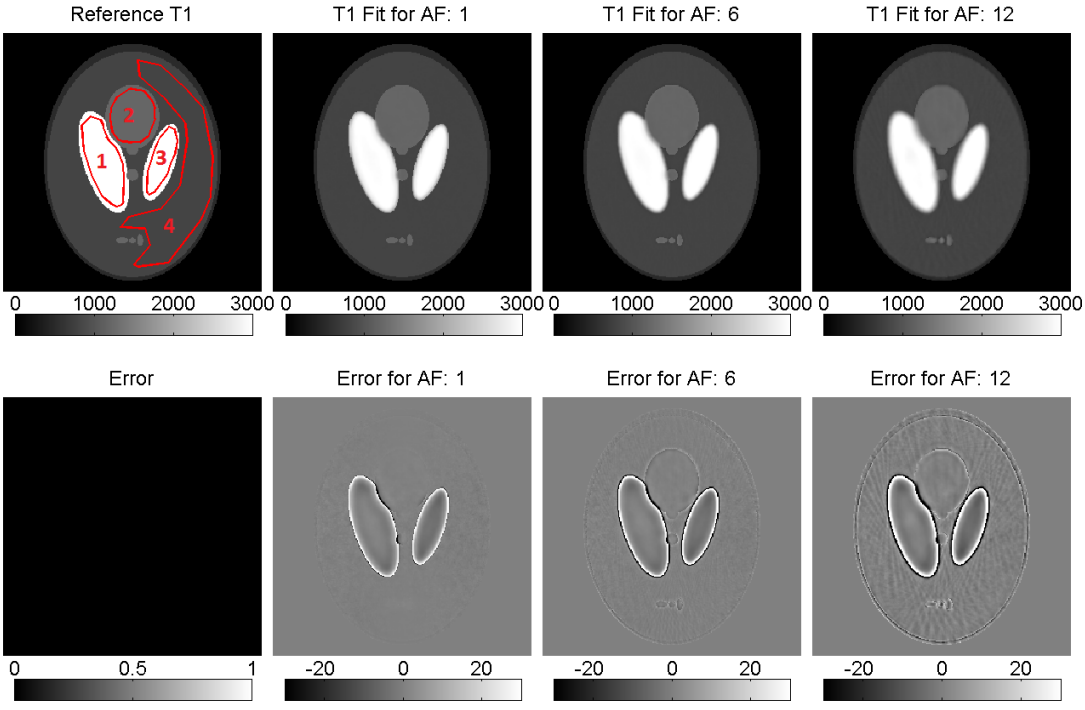

Figure 3.8: Estimated parameter maps of T_1 from the IRGN-TGV algorithm with a radial undersampling scheme and the corresponding fitting error in percent for different acceleration factors.

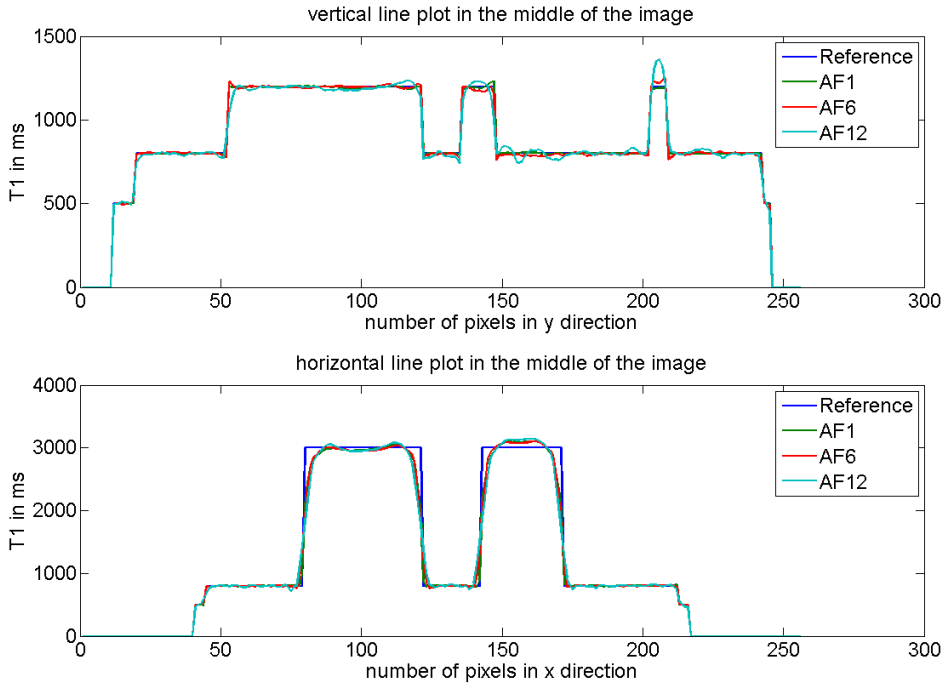

Figure 3.9: Line profile along the x- and y-axis of the resulting T_1 fit using a radial undersampling scheme for different acceleration factors and the IRGN-TGV algorithm. The center of the image is assumed to be the origin of the coordinate system.

Table 3.6: Mean and SD of the different ROIs and acceleration factors with a radial undersampling scheme of the numerical phantom and the IRGN-TGV algorithm. ROIs are defined as in Figure 3.8

	Reference T_1 mean in ms	Reference T_1 SD in ms	ACC 1 mean T_1 in ms	ACC 1 SD T_1 in ms
Roi 1	3000.000	0.000	2990.702	60.306
Roi 2	1200.000	0.000	1195.165	5.350
Roi 3	3000.000	0.000	3048.655	89.546
Roi 4	800.000	0.000	800.017	4.334
	ACC 6 mean T_1 in ms	ACC 6 SD T_1 in ms	ACC 12 mean T_1 in ms	ACC 12 SD T_1 in ms
Roi 1	3001.177	54.172	3011.871	83.411
Roi 2	1194.851	7.428	1195.207	15.806
Roi 3	3067.322	79.274	3079.189	136.500
Roi 4	799.894	6.107	799.622	10.856

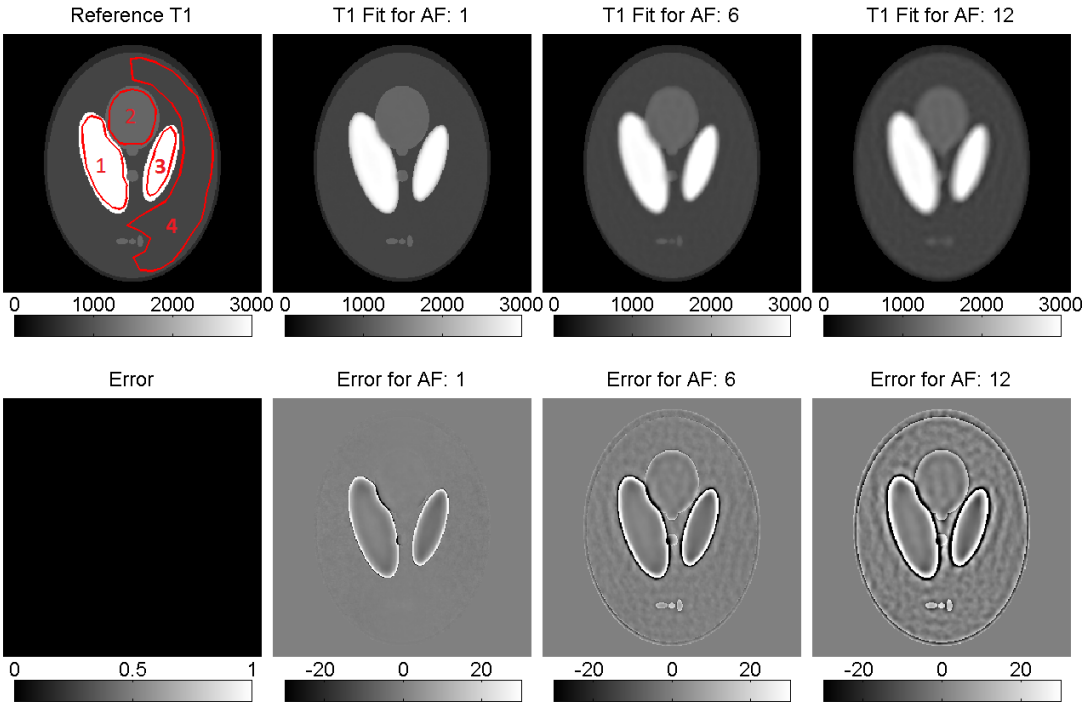

Figure 3.10: Estimated parameter maps of T_1 from the IRGN-TGV algorithm with a pseudo random undersampling scheme and the corresponding fitting error in percent for different acceleration factors.

Table 3.7: Mean and SD of the different ROIs and acceleration factors of the numerical phantom using a pseudo random undersampling scheme and the IRGN-TGV algorithm. ROIs are defined as in Figure 3.10

	Reference T_1 mean in ms	Reference T_1 SD in ms	ACC 1 mean T_1 in ms	ACC 1 SD T_1 in ms
Roi 1	3000.000	0.000	2971.849	85.872
Roi 2	1200.000	0.000	1195.457	5.991
Roi 3	3000.000	0.000	3054.480	82.048
Roi 4	800.000	0.000	799.945	4.312
	ACC 6 mean T_1 in ms	ACC 6 SD T_1 in ms	ACC 12 mean T_1 in ms	ACC 12 SD T_1 in ms
Roi 1	2959.439	132.118	2932.027	196.589
Roi 2	1197.745	23.982	1196.963	38.514
Roi 3	3060.543	109.316	3028.437	208.376
Roi 4	799.539	9.606	800.962	22.342

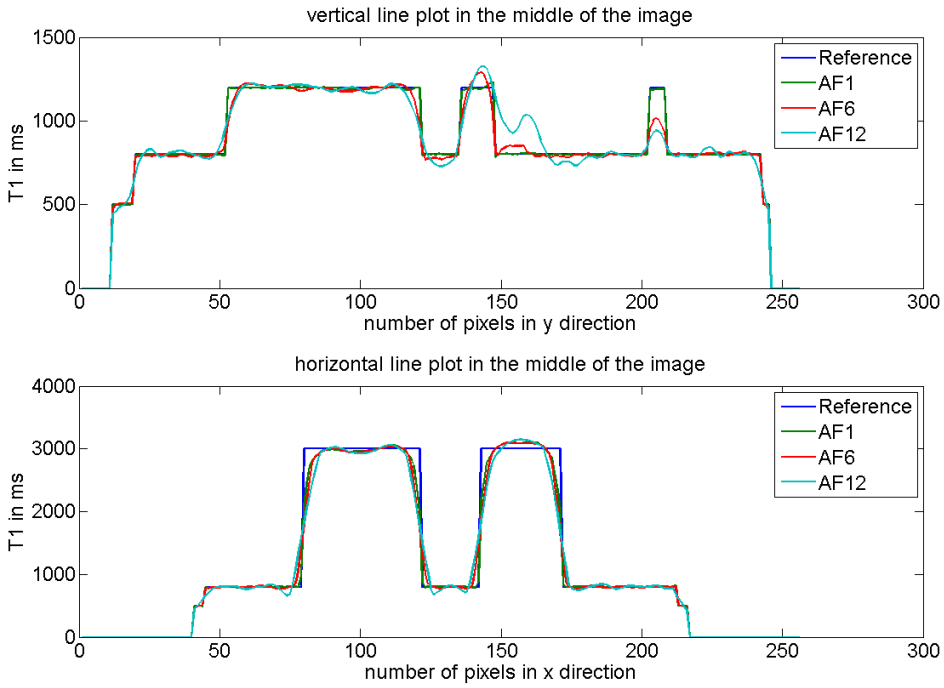

Figure 3.11: Line profile along the x- and y-axis of the resulting T_1 fit using a pseudo random undersampling scheme for different acceleration factors and the IRGN-TGV algorithm. The center of the image is assumed to be the origin of the coordinate system.

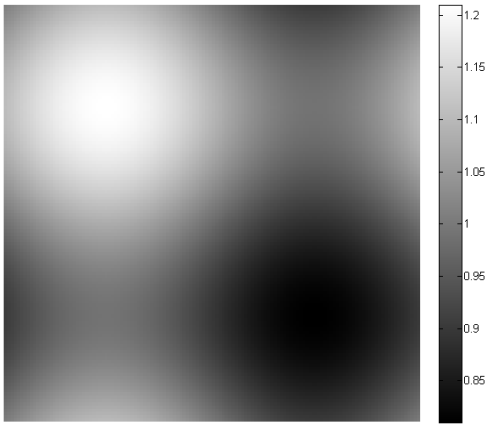

Figure 3.12: Simulated B_{1+} map for the numerical experiment of B_{1+} influence on the T_1 quantification.

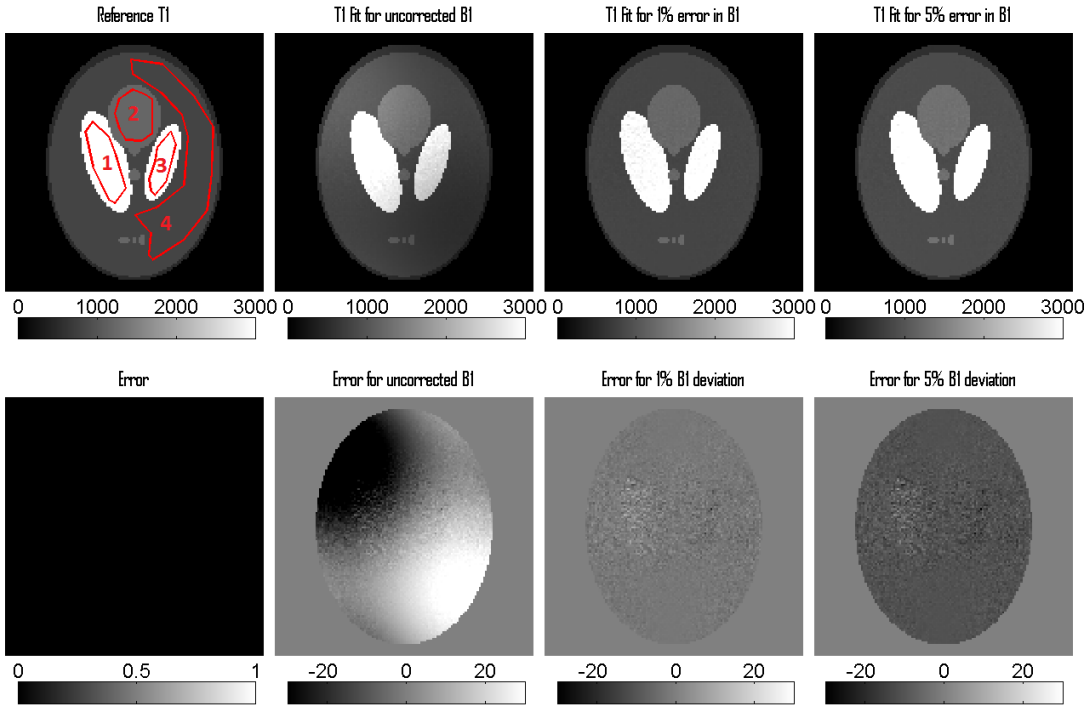

Figure 3.13: Resulting T_1 fit for different B_{1+} correction errors using the IRGN-TGV algorithm.

Table 3.8: Mean and SD of the different ROIs and B_{1+} maps of the numerical phantom and the IRGN-TGV algorithm. ROIs are defined as in Figure 3.13.

	Reference T_1 mean in ms	Reference T_1 SD in ms	Uncorrected B_{1+} mean in ms	Uncorrected B_{1+} SD in ms
Roi 1	3000.000	0.000	3317.916	380.702
Roi 2	1200.000	0.000	1400.529	85.386
Roi 3	3000.000	0.000	2616.376	174.869
Roi 4	800.000	0.000	667.648	116.613
	1% error in B_{1+} mean in ms	1% error in B_{1+} SD in ms	5% error in B_{1+} mean in ms	5% error in B_{1+} SD in ms
Roi 1	3013.657	108.277	3276.117	117.657
Roi 2	1219.867	23.969	1325.702	26.062
Roi 3	3087.511	98.765	3355.299	107.360
Roi 4	816.678	13.738	887.260	14.922

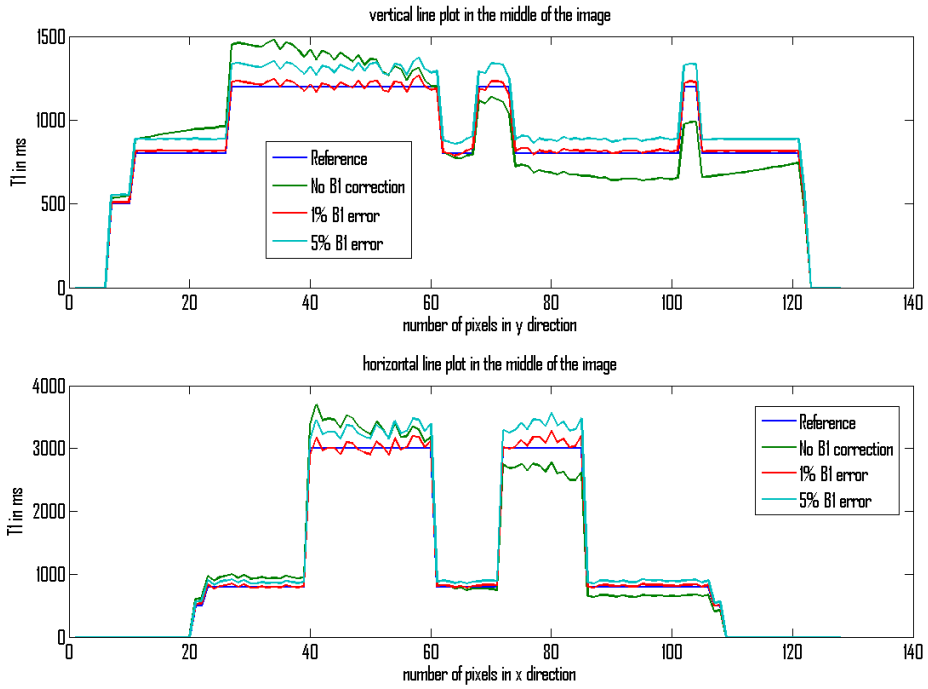

Figure 3.14: Line profile along the x- and y-axis of the resulting T_1 fit using different B_{1+} maps and the IRGN-TGV algorithm.

3.2 MRI phantom

All results were generated with the parameters for the IRGN-TGV algorithm as shown in Table 3.4. Turbo inversion recovery spin echo measurements of the different ROIs are shown in Table 3.11, sequence parameters are shown in Table 3.10. The sequence parameters of the used 3D-FLASH acquisition are shown in Table 3.9. All measurements were done on a 3T Siemens MAGNETOM Skyra.

Table 3.9: Sequence parameters for the 3D-FLASH acquisition of the MRI phantom measurements.

	T_R in ms	T_E in ms	α in °	FOV in mm	Scan matrix in a.u.	phase oversampling in %
Scan 1	7.27	2.6	3	256x256x208	256x256x208	15
Scan 2	7.27	2.6	10	256x256x208	256x256x208	15
Scan 3	7.27	2.6	16	256x256x208	256x256x208	15

Table 3.10: Sequence parameters for the turbo inversion recovery spin echo acquisition of the MRI phantom measurements.

T_I in ms	T_R in ms	T_E in ms	α in °	FOV in mm	Scan matrix in a.u.
80	10000	9.8	180	210x210	192x192
160	10000	9.8	180	210x210	192x192
300	10000	9.8	180	210x210	192x192
500	10000	9.8	180	210x210	192x192
800	10000	9.8	180	210x210	192x192
1200	10000	9.8	180	210x210	192x192
1800	10000	9.8	180	210x210	192x192
2480	10000	9.8	180	210x210	192x192

Table 3.11: Mean and SD of the different ROIs for the MRI phantom using an inversion recovery fit. ROIs are defined as in Figure 3.15

	Roi 1	Roi 2	Roi 3	Roi 4	Roi 5	Roi 6
T_1 mean in ms	660	389	215	1192	1081	3959
T_1 SD in ms	9	6	3	26	20	80

Interleaved pattern

The results for an interleaved undersampling pattern are shown in Figure 3.15. The image in the upper left corner of the figure represents the reference evaluated through a DESPOT1 fit. To the right of the reference is a fully sampled reconstruction generated with the IRGN-TGV algorithm and further to the right are the results for increased undersampling, namely 6 and 12 fold acceleration. The difference between the reference image and the accelerated reconstruction are illustrated below the corresponding parameter map and are given in percent. The mean and standard deviation for the different ROIs shown in Figure 3.15 were evaluated with Matlab and are presented in Table 3.12. The computation time for one reconstruction was approximately 8 hours on a 64 Bit Windows 7 PC with an Intel Core i5-3350p @ 3.10 GHz with 16 GB of RAM.

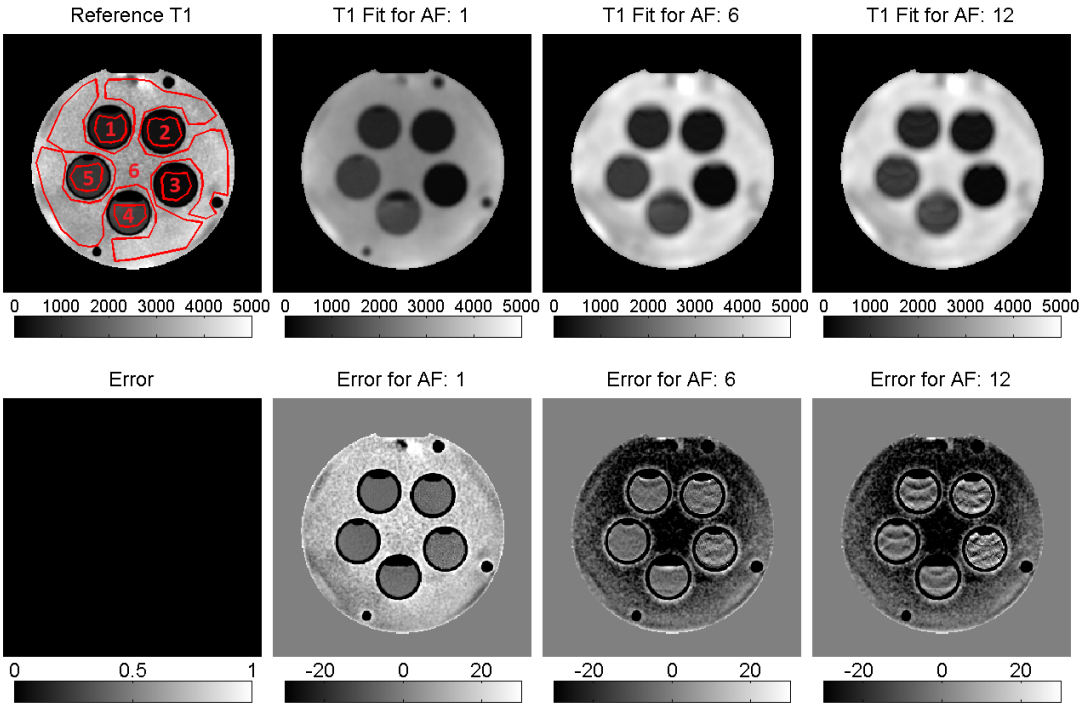

Figure 3.15: Estimated parameter maps of T_1 from the IRGN-TGV algorithm with an interleaved undersampling scheme and the corresponding fitting error in percent for different acceleration factors.

Table 3.12: Mean and SD of the different ROIs and acceleration factors of the MRI phantom using an interleaved undersampling scheme and the IRGN-TGV algorithm. ROIs are defined as in Figure 3.15

	Reference T_1 mean in ms	Reference T_1 SD in ms	ACC 1 mean T_1 in ms	ACC 1 SD T_1 in ms
Roi 1	647.759	20.505	680.891	23.431
Roi 2	355.022	9.364	371.095	17.033
Roi 3	186.369	5.751	191.831	10.196
Roi 4	1326.078	99.033	1383.255	105.350
Roi 5	1090.271	34.103	1140.414	28.745
Roi 6	3513.247	415.889	2999.869	325.097
	ACC 6 mean T_1 in ms	ACC 6 SD T_1 in ms	ACC 12 mean T_1 in ms	ACC 12 SD T_1 in ms
Roi 1	686.572	28.316	681.723	67.562
Roi 2	372.654	23.290	367.676	40.270
Roi 3	191.847	15.607	192.177	24.616
Roi 4	1388.959	108.202	1378.533	126.725
Roi 5	1143.305	25.911	1149.457	78.485
Roi 6	4143.072	372.139	4146.893	366.764

Table 3.13: Relative difference in percent of the mean T_1 values in Table 3.12 to the gold standard values in Table 3.11.

	Roi 1	Roi 2	Roi 3	Roi 4	Roi 5	Roi 6
ACC 1 difference in %	3.03	-4.63	-11.16	16.02	5.45	-24.25
ACC 6 difference in %	3.93	-4.37	-11.16	16.44	5.74	4.65
ACC 12 difference in %	3.18	-5.65	-10.70	15.6	6.29	4.72

Radial pattern

The results for a radial undersampling pattern are shown in Figure 3.16. The image in the upper left corner of the figure represents the reference evaluated through a DESPOT1 fit. To the right of the reference is a fully sampled reconstruction generated with the IRGN-TGV algorithm and further to the right are the results for increased undersampling, namely 6 and 12 fold acceleration. The difference between the reference image and the accelerated reconstruction are shown below the corresponding parameter map and are given in percent. The mean and standard deviation for the different ROIs shown in Figure 3.16 were evaluated with Matlab and are presented in Table 3.14. The computation

time for one reconstruction was approximately 8 hours on a 64 Bit Windows 7 PC with an Intel Core i5-3350p @ 3.10 GHz with 16 GB of RAM.

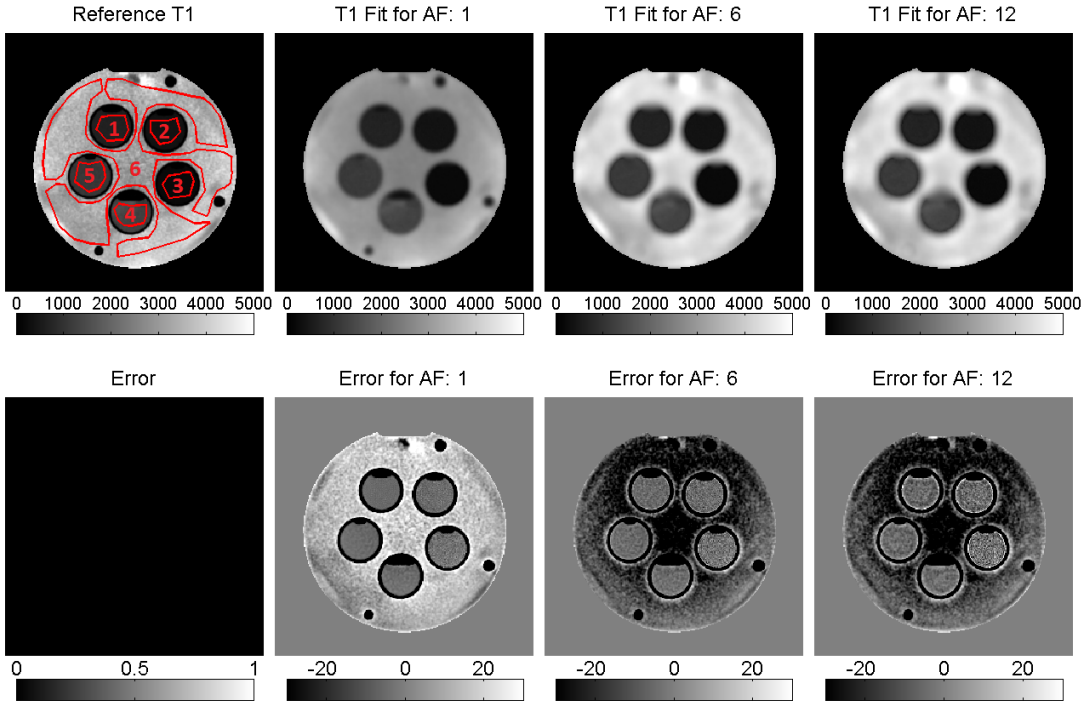

Figure 3.16: Estimated parameter maps of T_1 from the IRGN-TGV algorithm with a radial undersampling scheme and the corresponding fitting error in percent for different acceleration factors.

Pseudo random pattern

The results for a pseudo random undersampling pattern are shown in Figure 3.17. The image in the upper left corner of the figure represents the ground truth reference a DESPOT1 fit. To the right of the reference is a fully sampled reconstruction generated with the IRGN-TGV algorithm and further to the right are the results for increased undersampling, namely 6 times and 12 times acceleration. The difference between the reference image and the accelerated reconstruction are shown below the corresponding parameter map and are given in percent. The mean and standard deviation for the different ROIs shown in Figure 3.17 were evaluated with Matlab and are presented in Table 3.16. The

Table 3.14: Mean and SD of the different ROIs and acceleration factors of the MRI phantom using a radial undersampling scheme and the IRGN-TGV algorithm. ROIs are defined as in Figure 3.16

	Reference T_1 mean in ms	Reference T_1 SD in ms	ACC 1 mean T_1 in ms	ACC 1 SD T_1 in ms
Roi 1	648.060	20.666	681.243	23.608
Roi 2	354.798	9.002	370.677	16.446
Roi 3	186.770	5.835	191.811	10.138
Roi 4	1334.770	96.069	1391.095	102.114
Roi 5	1088.412	34.969	1140.426	29.753
Roi 6	3483.699	377.722	2983.475	301.631
	ACC 6 mean T_1 in ms	ACC 6 SD T_1 in ms	ACC 12 mean T_1 in ms	ACC 12 SD T_1 in ms
Roi 1	682.774	22.468	687.519	29.848
Roi 2	371.088	16.924	372.231	20.840
Roi 3	191.810	11.441	191.590	16.198
Roi 4	1394.166	101.764	1398.290	103.979
Roi 5	1142.521	30.675	1145.929	33.375
Roi 6	4148.048	351.516	4153.492	354.293

Table 3.15: Relative difference in percent of the mean T_1 values in Table 3.14 to the gold standard values in Table 3.11.

	Roi 1	Roi 2	Roi 3	Roi 4	Roi 5	Roi 6
ACC 1 difference in %	3.18	-4.88	-10.79	16.69	5.46	-24.65
ACC 6 difference in %	3.33	-4.63	-10.79	16.95	5.64	4.77
ACC 12 difference in %	4.09	-4.37	-10.89	17.37	6.01	4.90

computation time for one reconstruction was approximately 8 hours on a 64 Bit Windows 7 PC with an Intel Core i5-3350p @ 3.10 GHz with 16 GB of RAM.

3.3 In vivo knee measurements

The results for a pseudo random undersampling pattern are shown in Figure 3.18. The image in the upper left corner of the figure represents the reference evaluated through a DESPOT1 fit. To the right of the reference is a fully sampled reconstruction generated with the IRGN-TGV algorithm and further to the right are the results for increased

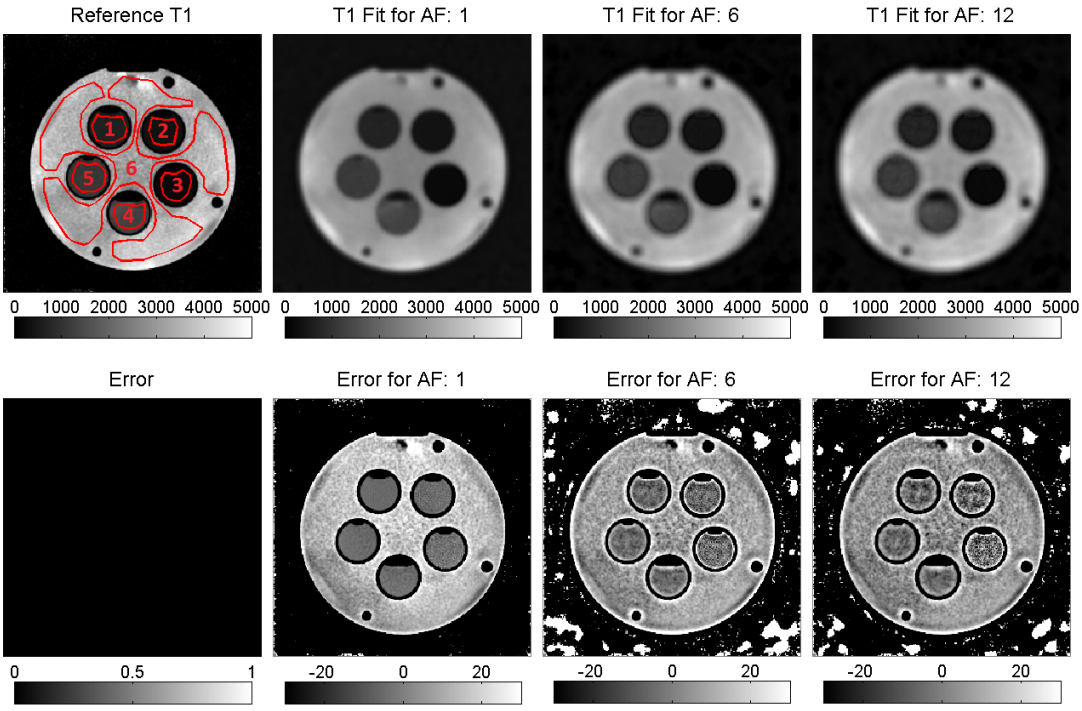

Figure 3.17: Estimated parameter maps of T_1 from the IRGN-TGV algorithm with a pseudo random undersampling scheme and the corresponding fitting error in percent for different acceleration factors.

undersampling, namely 6 and 12 fold acceleration. The difference between the reference image and the accelerated reconstruction are illustrated below the corresponding parameter map given in percent. The mean and standard deviation for the different ROIs shown in Figure 3.18 were evaluated with Matlab and are presented in Table 3.19. Additionally, all values are compared to the values found in literature [33, 34, 35], see Table 3.20. The computation time for one reconstruction was approximately 8 hours on a 64 Bit Windows 7 PC with an Intel Core i5-3350p @ 3.10 GHz with 16 GB of RAM. The sequence parameters of the used 3D-FLASH acquisition are shown in Table 3.18. All measurements were done on a 3T Siemens MAGNETOM Skyra.

Table 3.16: Mean and SD of the different ROIs and acceleration factors of the MRI phantom using a pseudo random undersampling scheme and the IRGN-TGV algorithm. ROIs are defined as in Figure 3.17

	Reference T_1 mean in ms	Reference T_1 SD in ms	ACC 1 mean T_1 in ms	ACC 1 SD T_1 in ms
Roi 1	649.190	21.079	682.087	23.868
Roi 2	354.918	9.229	371.102	16.327
Roi 3	186.319	5.818	191.755	10.348
Roi 4	1324.779	102.217	1381.223	109.577
Roi 5	1087.878	34.242	1139.591	28.627
Roi 6	3519.882	421.458	3012.068	316.303
	ACC 6 mean T_1 in ms	ACC 6 SD T_1 in ms	ACC 12 mean T_1 in ms	ACC 12 SD T_1 in ms
Roi 1	688.331	38.093	680.624	53.981
Roi 2	376.950	24.755	376.671	36.877
Roi 3	193.594	17.784	194.814	23.792
Roi 4	1386.915	116.540	1374.003	126.211
Roi 5	1140.334	44.661	1134.807	60.267
Roi 6	3242.360	271.919	3340.523	274.484

Table 3.17: Relative difference in percent of the mean T_1 values in Table 3.16 to the gold standard values in Table 3.11.

	Roi 1	Roi 2	Roi 3	Roi 4	Roi 5	Roi 6
ACC 1 difference in %	3.33	-4.63	-10.81	15.86	5.37	-23.92
ACC 6 difference in %	4.24	-3.08	-9.96	16.35	5.46	-18.11
ACC 12 difference in %	3.03	-3.34	-9.39	15.27	4.90	-15.64

Table 3.18: Sequence parameters for the 3D-FLASH acquisition of the in vivo knee measurements.

	T_R in ms	T_E in ms	α in °	FOV in mm	Scan matrix in a.u.	phase oversampling in %
Scan 1	6.18	2.46	3	180x180x145	256x256x208	15
Scan 2	6.18	2.46	10	180x180x145	256x256x208	15
Scan 3	6.18	2.46	16	180x180x145	256x256x208	15

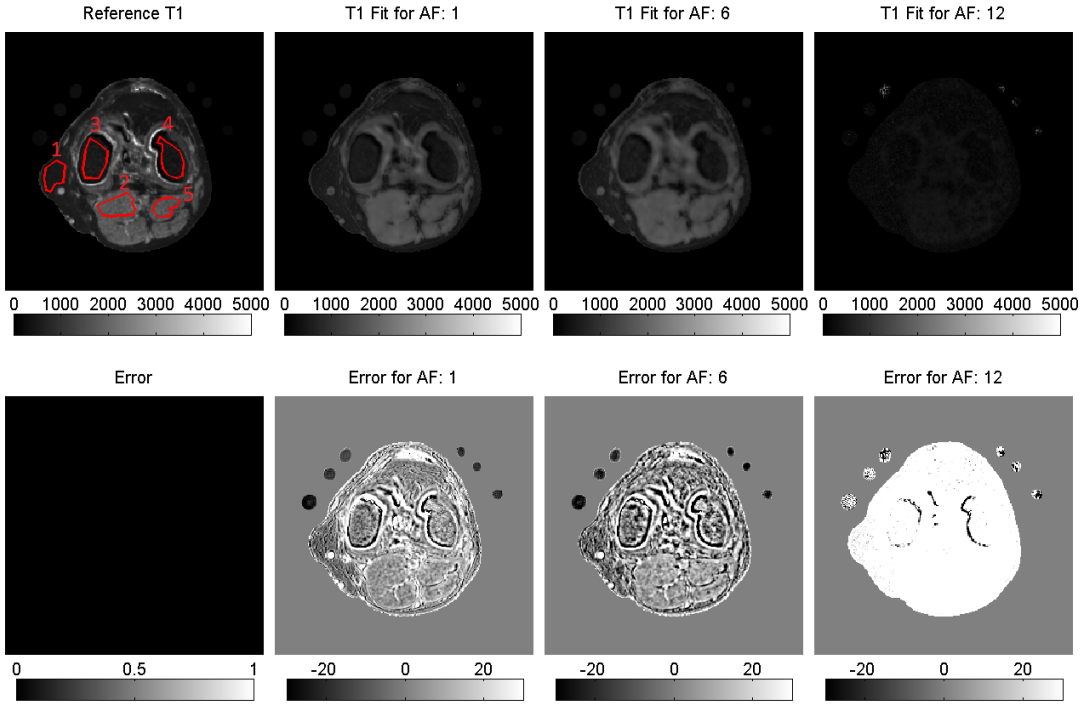

Figure 3.18: Estimated parameter maps of T_1 from the IRGN-TGV algorithm with a pseudo random undersampling scheme and the corresponding fitting error in percent for different acceleration factors.

Table 3.19: Mean and SD of the different ROIs and acceleration factors of the in vivo knee measurements using a pseudo random undersampling scheme and the IRGN-TGV algorithm. ROIs are defined as in Figure 3.18

	Reference T_1 mean in ms	Reference T_1 SD in ms	ACC 1 mean T_1 in ms	ACC 1 SD T_1 in ms
Roi 1	494.267	36.802	526.003	65.746
Roi 2	1725.262	110.238	1633.926	45.581
Roi 3	531.142	68.600	535.386	51.476
Roi 4	450.053	63.514	419.858	61.608
Roi 5	1623.165	130.858	1504.788	89.361
	ACC 6 mean T_1 in ms	ACC 6 SD T_1 in ms	ACC 12 mean T_1 in ms	ACC 12 SD T_1 in ms
Roi 1	528.088	66.680	211.818	124.911
Roi 2	1583.387	51.746	398.759	42.634
Roi 3	551.226	62.662	205.809	83.650
Roi 4	438.463	74.434	178.944	64.027
Roi 5	1481.615	71.543	371.157	66.426

Table 3.20: Reference T_1 values from literature for different tissues found in the human knee.

	Subcutaneous Fat	Skeletal Muscle	Tendons	Cartilage	Synovial Liquid	Blood	Marrow
	in ms	in ms	in ms	in ms	in ms	in ms	in ms
T_1	365±9[33]	1420±38.1[33] 1412±13[34]	621±23[35]	1240±107[33] 1156±10[34]	3620±320[33]	1932±85[34]	371±7.94[33]

Table 3.21: Relative difference in percent of the mean T_1 values in Table 3.19 to the values found for the relevant tissue in the literature.

	Roi 1 Fat	Roi 2 Muscle	Roi 3 Marrow	Roi 4 Marrow	Roi 5 Muscle
ACC 1 difference in %	44.11	15.07	44.20	12.93	5.92
ACC 6 difference in %	44.66	11.48	48.52	18.06	4.30
ACC 12 difference in %	-42.19	-71.97	-43.94	-52.02	-73.87

4 Discussion and Conclusion

4.1 IRGN-TGV algorithm

The reason for choosing the IRGN method as optimization algorithm is that it is easier to solve the linearized problem instead of operating directly on the non-linear problem. It is then possible to include more sophisticated regularization functionals in the linearized problem. A popular choice is the TGV-term but it adds the problem of being non smooth. An efficient solution for this type of problems can be computed with duality based approaches like the used Chambolle-Pock algorithm.

The algorithm proposed in Equation 2.36 has several parameters to optimize its performance. By increasing the regularization parameter λ the importance of the data term is increased and one has to find the optimal λ in order to stay true to the data but also regularize enough to minimize undersampling artifacts and noise. λ naturally depends on the noise-level and methods like Morozov's discrepancy principle [36] could be used to get estimates. Yet practical solutions in this work are achieved by computing reconstructions over a range of values and with visual evaluation of the image quality. In order to make λ independent of the measured data we normalize the measured data by the data L_2 norm times 100. In order to limit the maximum descent along the linearized function a penalty for the L_2 deviation of the function value is introduced. By increasing δ this penalty is given less weight and the minimization can walk further away from the linearization

point. In order to find the optimal δ one has to do the same trial and error procedure as with finding the optimal λ. The optimal TGV parameters $\alpha_0, \alpha_1, \beta_0, \beta_1$ are chosen by the recommendations proposed by Bredies et al. [30]. The primal(τ) and dual(σ) step sizes are chosen as recommended by Chambolle et al. [25] and are adapted in every step as described by Bredies et al. [31]. The chosen parameters yield a rather robust algorithm for a huge field of applications starting from numerical phantoms up to in vivo reconstructions with highly undersampled (up to factor 12) data. The agreement of the resulting fits with standard reconstruction is discussed in detail on the following pages.

Another crucial part in achieving a proper working algorithm is the scaling of the parameters. As T_1 scaling factor we choose the maximum T_1 value of the initial guess and divide every pixel by this value to receive a scaled T_1 map between 0 and 1. For highly undersampled data it is possible to obtain rather large numbers of T_1 due to the numeric instability of the DESPOT method which is used for computing an initial guess. To account for such outliers we limit the maximum T_1 scaling factor to 5000 because there exists no tissue of interest with higher T_1 values in vivo. The M_0 scaling factor is chosen based upon a histogram driven approach because M_0 has no physical limitations similar to T_1.

By using the appropriate scaling factors and parameters for the algorithm it even is possible to initialize the optimization algorithm with a flat initial guess. This is a huge advantage over the CG_descent algorithm because the initial guess for higher acceleration factors is quite erroneous and these errors have a huge influence on the convergence of the algorithm. Yet a good initial guess improves the convergence rate to the optimal solution significantly. However, no effects on the accuracy of the fit could be observed.

Furthermore, a good estimate of the flip angle distribution across the slice is needed to produce accurate results. Even slight deviations of the flip angle lead to huge errors in the T_1 map, as can be seen in Figure 3.13 and 3.14. Simulating B_{1+} deviations in the order of 5%, which is a reasonable error for in vivo B_{1+} maps, lead to T_1 errors of up to 15%,

see Table 3.8. Therefore, it is crucial to achieve flip angle maps as accurate as possible to achieve reliable T_1 maps.

To account for problems concerning inexact slice profiles all measurements are done with 3D-sequences. 3D slabs still suffer from a non perfect slice profile at the edges of the volume, therefore reconstruction is performed on the inner slices only. The reconstruction is done by 1D-Fourier transform along the read-out direction followed by performing the optimization algorithm on the 2D slices generated by the 1D transform. This is necessary due to RAM limitations of the currently available hardware. In order to show the good performance of the algorithm and due to the long reconstruction time of more than 8 hours per slice and per acceleration case only the middle slice of the 3D volume is reconstructed. Choosing the middle slice is also the best choice regarding the slice profile along the 3D volume due to the fact that the outer slices are not reaching the nominal flip angle. The reason for this problem is the inability to produce RF-pulse that excite an exactly rectangular volume.

4.2 CG_descent

The CG_descent algorithm needs the first derivative of the cost function in every step in order to minimize the problem. Therefore it is limited to smooth regularization terms, e.g. the Tikhonov regularization. A regularization term is necessary because of the ill-posedness of the problem increases with increasing acceleration. The simple Tihkhonov regularization provides a stability increase of the problem at the cost of loosing sharp edges. In order to overcome this drawback we reduce the corresponding λ by a factor of 10 after each restart. This yields a strong regularized algorithm far away from the optimal solution and little to no regularization close to the optimal solution. The CG_descent algorithm of Hager et al. [26] has the advantage of automatically switching between a LBFGS optimization algorithm to a CG algorithm if the program runs out of memory.

The same scaling for the data and parameters as well as the same initial guess as for IRGN-TGV are used to make both approaches comparable. As shown in Figure 3.4 the CG_descent algorithm was unable to converge to the optimal solution. However, this is not surprising for a non-linear, non-convex problem because there is no theoretical proof of convergence for these problems. Because of the poor performance of the CG_descent algorithm on numerically simulated data even for no acceleration it is not used any further for the problems at hand. It has to be noted that the algorithm was able to converge with an initial guess close to the solution. Because of the superior performance of the IRGN-TGV algorithm this approach was not further investigated.

4.3 Numerical simulations

The results for no acceleration show good agreement with the reference T_1, both in absolute T_1 value in the different ROIs as well as at the edges of different tissues, see Tables 3.5, 3.6, 3.7. The error maps in Figures 3.6- 3.10 as well as the line plots along the x- and y axis in Figures 3.7- 3.11 supplement the good agreement but also show that the higher the difference at the border of two tissues, the higher the error of the resulting fit in that specific region. This is due to the fact that the TGV regularization term has increasing costs for higher jumps as can be seen in Figure 4.1. The fact that a higher jump cost more in terms of minimization yields to a piecewise smooth signal behavior at edges with very distinct T_1 values. This effect can be seen by taking a closer look at the line plots for different acceleration factors. At low acceleration factors there is little noise in the image and thus the edges can be clearly detected. The higher the acceleration, the higher the noise and at some point it is more cost efficient in terms of minimization to fit a line between two points close to the edge instead of a jump. This yields a blurring of edges especially in regions of very distinctive T_1 values. A possible solution might be the use of modifications to TGV that avoid step-dependent increase of cost.

Another important part is the choice of the undersampling pattern. Undersampling patterns that result in the best possible incoherence of the aliasing artifacts in the image domain (radial, Poisson disk, random) are favorable over sampling pattern that yield coherent aliasing (uniform Cartesian, block pattern) and thus leading to high image degradation for already modest acceleration factors. This results in typical residual artifacts, shown in Figure 3.6, even for moderate acceleration factors like 6. For higher acceleration factors it was impossible to reconstruct a valid parameter map. Therefore, a pattern with better incoherence condition should be chosen. A pattern which is easy to implement in practice is the radial undersampling know from projection methods like the CT. By using this pattern it is possible to reconstruct the T_1 map even at high acceleration of 12 with good accuracy and little residual artifacts. Taking a closer look at the error maps in Figure 3.8 one can see the typical residual artifacts of a radial pattern, the so called streaking artifacts. They get more pronounced at higher acceleration rates. At an undersampling factor of 6 they are barely visible. However, at 12 they can be clearly seen in the error map although they are nearly not present in the T_1 map itself.

The best choice for the undersampling pattern is a pseudo random undersampling scheme because it minimizes residual artifacts related to the pattern itself. The results for such an undersampling pattern are shown in Figure 3.10. Even for high acceleration factors the residual artifacts have the nature of noise and no characteristic patterns are recognizable in either the T_1 maps themself or the error maps. Even though this pattern offers huge advantages regarding the quality of the resulting reconstruction it has the major drawback that it is not commonly available on conventional clinical MRI scanners. Furthermore, the results for the pseudo random pattern are slightly worse than the ones for the radial pattern especially at edges which could be due to the fact that the radial pattern is rotated for every flip angle in order to maximize the k-space information. By generating three different random patterns for the three flip angles used, a result similar to the radial pattern can be expected. The reconstructed T_1 maps show good agreement with the reference for all acceleration factors and patterns in the four defined ROIs except for the inter-

leaved pattern at the highest acceleration factor. The mean pixel value of the reference always lies within one standard deviation around the mean of the reconstructed T_1 map. As expected the standard deviation increases with increasing acceleration because the overall SNR of the fit decreases with increasing acceleration. Additionally the percentual standard deviation varies along different tissues. A higher T_1 leads to a higher standard deviation. This is due to the fact that the minimization algorithm produces blurring at edges relative to the change in the absolute value by fitting of a smooth function between the edges of a tissue, as can be seen in Figure 3.11 in the plot along the x-axis. The two jumps to a tissues with a T_1 of 3000ms results in a smooth signal behavior between the edges with even a slightly over shoot. As explained above, the reason might be a shortcoming of the TGV functional.

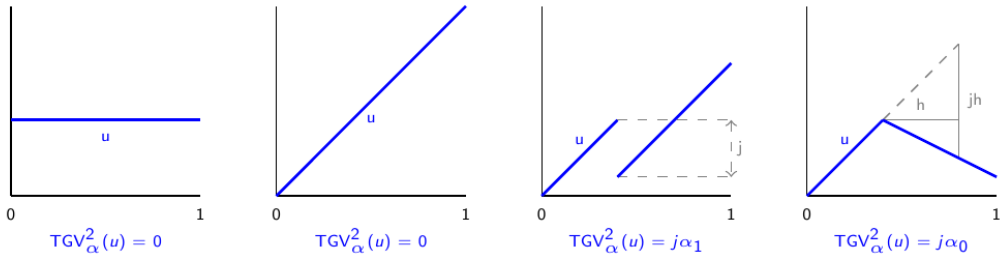

Figure 4.1: Value of the TGV functional for different functions in 1D. Constant and linear functions have zero cost, discontinuities depend upon the jump distance respectively the turn rate.

4.4 MRI phantom

In order to show the robustness of the algorithm the results for the MRI phantom measurements are generated with the same parameters as in the numerical case. Even though they are not optimized for the MRI data the results are very promising and show good agreement with the fully sampled reference. Taking a closer look at the parameter maps for the interleaved pattern in Figure 3.15, there are little to no residual artifacts of the

used pattern up to a acceleration factor of 6. At a speed up factor of 12 they become visible but only in the small tubes. The absolute values of the different tubes differ only to a small percentage (up to 2.5%) from the reference values but the T_1 of the surrounding water was significantly overestimated by up to 30%. The results for the radial pattern in Figure 3.16 show also a good agreement with the reference values within the tubes and an overestimation of the T_1 of the surrounding water. In contrast to the interleaved pattern there are no residual artifacts corresponding to the used pattern visible. The pseudo random pattern performed best for the measured data, having the lowest fitting error of all the used patterns through all acceleration factors. It was not possible to reconstruct the small borders of the acrylic glass tubes due to the effects involved at borders of highly distinct T_1 values described in section 4.3.

Taking a closer look a the mean and standard deviation in the six different ROIs it is interesting to note that the standard deviation of ROIs with high T_1 values stays nearly the same for all acceleration factors and is even better than the reference standard deviation in water. The smaller the absolute T_1 value the higher the increase in the standard deviation with increasing acceleration. Therefore the SNR of the reconstructed parameter map is dependent on the absolute value of T_1 in the tissue of interest. The small deviations in reference values between the different patterns are due to the fact that the ROIs are drawn independent from each other for every pattern, e.g. all ROIs are the same within the interleaved pattern but are different to those of the radial pattern.

Comparing the results of the IRGN-TGV fit to those of the inversion recovery spin echo experiment in Table 3.11 reveals some deviations of the proposed method to the reference T_1 values for all acceleration factors. The relative differences for the different acceleration factors in Table 3.13, 3.15 and 3.17 show a good agreement with the gold standard for moderate T_1 values. Small T_1 values < 300 ms and large T_1 values > 1100ms show substantial difference to the gold standard of more than 10%. Another finding is that small values are underestimated, whereas high T_1 values are generally overestimated except for water. The results for water in the inversion recovery spin echo experiment are likely

erroneous because of the very long T_1 of water and the relatively short T_R of 10s chosen for the inversion recovery sequence. To produce accurate results the T_R should be in the order of 5 times the maximum T_1 of the investigated substance. Literature suggests a water T_1 of 4200-4500ms which clearly violates this assumption.

Possible explanations for the difference to the gold standard method are errors in the calculated B_{1+}-map which result in wrong flip angles in that region, a problem present in all VFA methods. Even a slight deviation of the flip angle leads to huge errors in the resulting T_1 map. The results in Section 3.1.4, as well as the discussion of those results in section 4.1, promote this assumption. Therefore, it is crucial to generate a B_{1+}-map as accurate as possible. Furthermore, errors in the coil sensitivity map can lead to under- or overestimation of the resulting T_1 map.

4.5 In vivo reconstruction

The in vivo results are generated using the same parameters for the optimization algorithm as in the numerical and MRI phantom set-up. Because the random pattern performed best with real MRI data, as can be seen in the previous section, it is used to show the performance of the algorithm on in vivo data. The reconstructed T_1 map for fully sampled data shows good edge information as well as preserved small structures in adipose tissue. The error map in Figure 3.18 supports this finding by clearly showing detail information which is present in the IRGN reconstruction but absent in the DESPOT1 fit, most likely due to the TV denoising. Comparing the absolute values of the reconstructed T_1 map to those of the literature shows that the algorithm overestimates T_1 for all tissues of interest as can be seen in Table 3.21. However the DESPOT method yields values similar to the ones found by our algorithm. This suggests that the reason for the deviations can be found in the acquired data or the used preprocessing. Possible problems are the already discussed sensitivity to errors in the flip angle map as well as errors in the computed coil

sensitivities. The flip angles where chosen as proposed by Cheng et al. [7]. However, it is not yet clear if the chosen flip angles are optimal in the sense of maximizing the distinct information in the measurement data for our reconstruction. The algorithm performs well up to an acceleration of six, even preserving detail information, but breaks down if further acceleration is applied even though it was possible to reconstruct phantoms with an acceleration of 12.

4.6 Conclusion

The presented work describes a new algorithm to solve a T_1 parameter fitting problem based upon the VFA method. Due to the general formulation of the algorithm it is extendable and can therefore be used for all different kinds of model-based optimization problems. Additionally the proposed technique is robust regarding the choice of optimization parameters as observed for numerical simulations, phantom data, and in vivo applications.

It is further shown that the accuracy of VFA parameter mapping is strongly influenced by the accuracy of the B_{1+} map. Further research has to be done in order to produce more accurate flip-angle mapping techniques as well as validate existing methods.

The rather long reconstruction times of up to eight hours per slice gives rise to the need of acceleration. This could be done by porting the code from the CPU to the GPU.

The blurring in regions of strong signal changes may be solved by adapting the TGV regularization to account for different increments of intensity.

Bibliography

[1] Tofts PS and Kermode AG. “Measurement of the blood-brain barrier permeability and leakage space using dynamic MR imaging. 1. Fundamental concepts.” In: *Magnetic Resonance in Medicine* 17.2 (1991), pp. 357–367.

[2] Larsson HB, Stubgaard M, et al. “Quantitation of blood-brain barrier defect by magnetic resonance imaging and gadolinium-DTPA in patients with multiple sclerosis and brain tumors.” In: *Magnetic Resonance in Medicine* 16.1 (1990), pp. 117–131.

[3] Hulka CA, Smith BL, et al. “Benign and malignant breast lesions: differentiation with echo-planar MR imaging”. In: *Radiology* 197.1 (1995), pp. 33–38.

[4] GJM Parker, Suckling J, et al. “Probing tumor microvascularity by measurement, analysis and display of contrast agent uptake kinetics”. In: *Journal of Magnetic Resonance Imaging* 7.3 (1997), pp. 564–574.

[5] den Boer JA, Hoenderop RKKM, et al. “Pharmacokinetic analysis of Gd-DTPA enhancement in dynamic three-dimensional MRI of breast lesions.” In: *Journal of magnetic resonance imaging* 7.4 (1997), pp. 702–715.

[6] Gore JC, Kang YS, and Schulz RJ. “Measurement of radiation dose distributions by nuclear magnetic resonance (NMR) imaging.” In: *Physics in medicine and biology* 29.10 (1984), pp. 1189–1197.

[7] Cheng HLM and Wright GA. “Rapid high-rsolution T1 mapping by variable flip angles: Accurate and precise measurements in the presence of radiofrequency field inhomogeneity”. In: *Magnetic Resonance in Medicine* 55.3 (2006), pp. 566–574.

[8] Look DC and Locker DR. "Time saving in measurement of NMR and EPR relaxation times". In: *Review of Scientific Instruments* 41.2 (1970), pp. 250–251.

[9] Crawley AP and Henkelman RM. "A comparison of one-shot and recovery methods in T1 imaging." In: *Magnetic Resonance in Medicine* 7.1 (1988), pp. 23–34.

[10] Henderson E, McKinnon G, et al. "A fast 3D look-locker method for volumetric T1 mapping". In: *Magnetic Resonance Imaging* 17.8 (1999), pp. 1163–1171.

[11] Deoni SCL, Peters TM, and Rutt BK. "High-resolution T1 and T2 mapping of the brain in a clinically acceptable time with DESPOT1 and DESPOT2". In: *Magnetic Resonance in Medicine* 53.1 (2005), pp. 237–241.

[12] DR Messroghli, Radjenovic A, et al. "Modified look-locker inversion recovery (MOLLI) for high-resolution T 1 mapping of the heart". In: *Magnetic Resonance in Medicine* 52.1 (2004), pp. 141–146.

[13] Schmitt P, Griswold MA, et al. "Inversion recovery TrueFISP: quantification of T(1), T(2), and spin density." In: *Magnetic Resonance in Medicine* 51.4 (2004), pp. 661–667.

[14] Scheffler K. "On the transient phase of balanced SSFP sequences". In: *Magnetic Resonance in Medicine* 49.4 (2003), pp. 781–783.

[15] Lesch A. "Quantification of T1, T2 and Pseudo Spin Density using bSSFP with Correction for Non-Ideal Flip Angle Profiles". 2014.

[16] Deoni SCL, Rutt BK, and Peters TM. "Rapid combined T1 and T2 mapping using gradient recalled acquisition in the steady state". In: *Magnetic Resonance in Medicine* 49.3 (2003), pp. 515–526.

[17] Ma D, Gulani V, et al. "Magnetic resonance fingerprinting". In: *Nature* 495.7440 (2013), pp. 187–192.

[18] Tran-Gia J, Wech T, et al. "Model-Based Acceleration of Look-Locker T1 Mapping". In: *Plos One* 10.4 (2015), e0122611.

[19] Sumpf T. "Model-based T 2 Relaxometry using Undersampled Magnetic Resonance Imaging". In: (2012).

[20] Sumpf TJ, Petrovic A, and Uecker M. "Fast T2 Mapping with Improved Accuracy Using Undersampled Spin-echo MRI and Model-based Reconstructions with a Generating Function". In: *IEEE Transactions on Medical Imaging* (2014), p. 10.

[21] Walsh DO, Gmitro AF, and Marcellin MW. "Adaptive reconstruction of phased array MR imagery". In: *Magnetic Resonance in Medicine* 43.5 (2000), pp. 682–690.

[22] M Uecker, Hohage T, et al. "Image reconstruction by regularized nonlinear inversion - Joint estimation of coil sensitivities and image content". In: *Magnetic Resonance in Medicine* 60.3 (2008), pp. 674–682.

[23] Stollberger R and Wach P. "Erratum: Imaging of the active B1 field in vivo (Magnetic Resonance in Medicine (1996) 35 (246-251))". In: *Magnetic Resonance in Medicine* 38.2 (1997), p. 336.

[24] Sacolick LI, Wiesinger F, et al. "B1 mapping by Bloch-Siegert shift". In: *Magnetic Resonance in Medicine* 63.5 (2010), pp. 1315–1322.

[25] Chambolle A and Pock T. "A first-order primal-dual algorithm for convex problems with applications to imaging". In: *Journal of Mathematical Imaging and Vision* May (2010). URL: `http://gpu4vision.icg.tugraz.at/papers/2010/pock_primal_dual.pdf`.

[26] Hager WW and Zhang H. "Algorithm 851: CG_DESCENT, a conjugate gradient method with guaranteed descent". In: *ACM Transactions on Mathematical Software (TOMS)* 32.1 (2006), pp. 113–137.

[27] Hager WW and Zhang H. "A survey of nonlinear conjugate gradient methods". In: *Pacific Journal of Optimization* 2.1 (2006), pp. 35–58.

[28] Hager WW and Zhang H. "A New Conjugate Gradient Method with Guaranteed Descent and an Efficient Line Search". In: *SIAM Journal on Optimization* 16.1 (2005), pp. 170–192.

[29] J Nocedal. "Updating quasi-Newton matrices with limited storage". In: *Mathematics of Computation* 35.151 (1980), pp. 773–773.

[30] Bredies K, Kunisch K, and Pock T. "Total Generalized Variation". In: *SIAM Journal on Imaging Sciences* 3.3 (2010), pp. 492–526.

[31] Bredies K and Holler M. "A TGV-based framework for variational image decompression , zooming and reconstruction . Part II: Numerics". In: *Journal on Imaging Sciences* (2015). URL: `https://www.ma.tum.de/foswiki/pub/IGDK1754/Preprints/BrediesHoller_2015B.pdf`.

[32] Guerquin-Kern M. *Matlab MRI Phantom*. 2012. URL: `http://bigwww.epfl.ch/algorithms.html` (visited on 12/14/2015).

[33] Han E, Gold G, et al. "In-Vivo T1 and T2 Measurements of Muskuloskeletal Tissue at 3T and 1.5T". In: *International Society for Magnetic Resonance in Medicine* (2003).

[34] Stanisz GJ, Odrobina EE, et al. "T1, T2 relaxation and magnetization transfer in tissue at 3T". In: *Magnetic Resonance in Medicine* (2005).

[35] Filho GH, Du J, et al. "Quantitative characterization of the Achilles tendon in cadaveric specimens: T1 and T2* measurements using ultrashort-TE MRI at 3 T". In: *American Journal of Roentgenology* (2009).

[36] Morozov VA. "On the solution of functional equations by the method of regularization". In: *Soviet Mathematics Doklady* (1966).

List of Figures

List of Tables